



HAL
open science

Chemical erosion rates in the upper Blue Nile Basin and related atmospheric CO₂ consumption

Luc Bastian, Nathalie Vigier, Marie Revel, Gezahegn Yirgu, Dereje Ayalew,
Raphaël Pik

► **To cite this version:**

Luc Bastian, Nathalie Vigier, Marie Revel, Gezahegn Yirgu, Dereje Ayalew, et al.. Chemical erosion rates in the upper Blue Nile Basin and related atmospheric CO₂ consumption. *Chemical Geology*, 2019, 518, pp.19-31. 10.1016/j.chemgeo.2019.03.033 . hal-02134565

HAL Id: hal-02134565

<https://hal.science/hal-02134565>

Submitted on 22 Oct 2021

HAL is a multi-disciplinary open access archive for the deposit and dissemination of scientific research documents, whether they are published or not. The documents may come from teaching and research institutions in France or abroad, or from public or private research centers.

L'archive ouverte pluridisciplinaire **HAL**, est destinée au dépôt et à la diffusion de documents scientifiques de niveau recherche, publiés ou non, émanant des établissements d'enseignement et de recherche français ou étrangers, des laboratoires publics ou privés.



Distributed under a Creative Commons Attribution - NonCommercial 4.0 International License

20 **Abstract**

21

22 Silicate weathering of basaltic rocks constitutes a non-negligible sink of atmospheric CO₂ but
23 the role it plays in the regulation of past and future global climate is still matter of debate. In
24 this study, silicate weathering rates for various sub-basins of the Ethiopian Traps, emplaced
25 30 million years ago, and the corresponding atmospheric CO₂ consumption rates are
26 evaluated. For this, major and trace elements were measured in the dissolved phases and in
27 the sedimentary particles carried and deposited by the main rivers flowing through this steep
28 region. Lithium isotopes and major elements were also measured in the extracted clay
29 fractions in order to infer complementary information on weathering processes in this region.
30 Clay $\delta^7\text{Li}$ values correlate positively with Mg/Ti ratios, and are best explained by varying
31 ratios of leaching versus clay formation rate.

32 Although located in a region annually submitted to monsoon, average silicate weathering rate
33 (16.1 tons/km²/year) and CO₂ consumption rate (0.65×10^{12} mol/year) are estimated to be low
34 when compared to other basaltic regions such as the Deccan Traps, and volcanically active
35 islands of the tropical zone. This is surprising since the concentrations of Total Dissolved
36 Solids of the Ethiopian rivers are among the highest ones. With a 2D rainfall model that takes
37 into account the detailed topography of the region, annual occurrence of the Monsoon, and
38 monitoring station data, we show that runoff intensity is a key parameter that explains this
39 difference. We determine that, at present, the weathering of the Ethiopian Traps plays a
40 negligible role in the carbon cycle. However, simple calculations, which integrate recent
41 knowledge on African climate variations and on weathering controls, illustrate that during the
42 African Humid Period (14-8 kyr), a significant increase of Monsoon precipitation may have
43 resulted in much higher weathering rates and related CO₂ consumption ($0.91-1.5 \times 10^{12}$
44 mol/year). This study therefore evidences the potential importance of this region in the past,
45 and the need to quantify more precisely the variations of the monsoon intensity and its impact
46 on tropical watersheds for reconstructing past CO₂ levels.

47

48

49 **Key words**

50

51 Ethiopian Traps, silicate weathering rate, lithium isotopes, CO₂ consumption, basalt, African
52 monsoon

53

54 **1. Introduction**

55

56 Chemical and physical erosion, which describe respectively mineral dissolution and soil
57 formation, rock cracking and particle transport are key processes in landscape evolution.
58 Various parameters can control weathering (chemical erosion) at a watershed scale, among
59 them lithology, tectonics, relief, soil thickness, age, vegetation cover and climate parameters
60 (Bayon et al., 2016; Bouchez et al., 2013; Brady et al., 1999; Clergue et al., 2015; Dessert et
61 al., 2001; Gaillardet et al., 1999; Li et al., 2016; P Louvat and Allègre, 1998; West et al.,
62 2005). Over geological timescale ($>10^5$ years), silicate weathering, with organic matter burial,
63 are major sinks of atmospheric carbon. Weathering of silicate rocks consumes atmospheric
64 CO_2 and transforms it to dissolved HCO_3^- (Gaillardet et al., 1999), which further precipitates
65 with calcium carbonate in the ocean. As CO_2 is a greenhouse gas, silicate rock weathering can
66 be a critical feedback control on the climate (Brady and Carroll, 1994; Walker et al., 1981).
67 However, at present, the relative importance of the various continental areas and various types
68 of lithologies having played a key role in the carbon cycle is still debated, in particular over
69 the Cenozoic. The emplacement of the Himalayas (and its uplift) may have been critical but
70 this is not consensual thus far. Other mountainous regions may have been of importance, in
71 particular those rich in basaltic lithologies, and are little considered yet (Li and Elderfield,
72 2013). Indeed, all silicate rocks do not present the same sensitivity to weathering. Among
73 them, basaltic rocks can be weathered more easily than any other igneous ones (e.g. Dessert et
74 al., 2003). Some studies (Dessert et al., 2003; Gaillardet et al., 1999; Louvat and Allègre,
75 1997; P Louvat and Allègre, 1998) indicate that basaltic rocks are weathered 8 time faster
76 than granitic rocks. Millot et al., (2002) show that the silicate weathering rate is 10 to 100
77 times larger for basaltic regions than for granitic areas. Basalt weathering has thus been
78 estimated as an important sink of CO_2 at the global scale (Dessert et al., 2003) and it is
79 calculated to be responsible of 30% of the present-day CO_2 consumption (Gaillardet et al.,
80 1999). The Deccan Traps were investigated in great details (e.g. Das et al., 2005; Dessert et
81 al., 2001; Kisakürek et al., 2004; Vigier et al., 2005), as well as the Siberian Traps (e.g.
82 Pokrovsky et al., 2005; Zakharova et al., 2005). However, some large basaltic provinces have
83 not been studied yet. For example, weathering of the Ethiopian Traps (upper Blue Nile Basin)
84 is not well constrained, despite the importance of this region in terms of climate, size,
85 tectonics and age (30 Ma). A recent carbon-climate modeling study highlights that the
86 Ethiopian Traps were the world-wide most important hotspot of silicate weathering during the
87 Oligocene (Lefebvre et al., 2013). The invoked reason is that, during this period, the

88 Ethiopian Traps were located within the equatorial latitudes, affected by high precipitation
89 rates and high temperatures, two parameters known to strongly increase basaltic weathering
90 rates (Dessert et al., 2003; Godd ris et al., 2013). At present the Ethiopian Traps are
91 influenced by monsoonal climate, with most precipitation occurring during the summer
92 period. The monsoon intensity in North-East Africa fluctuated significantly in the past, with,
93 for instance, particularly high peaks during high insolation periods such as the African Humid
94 period (14.5 to 8 ka, (Lamb et al., 2018; Shanahan et al., 2015)). Numerous studies show that
95 monsoon variations controlled physical erosion and the Blue Nile sediment flux during the
96 Quaternary period (Revel et al., 2015, 2014, 2010). As shown by lithium isotope data for the
97 Nile Basin (Bastian et al., 2017) and for the Himalayas (Dosseto et al., 2015), or hafnium
98 isotopes for the Congo Basin (Bayon et al., 2012), continental silicate weathering can respond
99 rapidly to monsoon fluctuations. Thus, the impact of the Ethiopian Traps on the atmospheric-
100 ocean carbon system deserves to be assessed both at present and in the past.

101 In fact, from sedimentary records located in the Nile deep sea fan, the importance of physical
102 erosion in this region, and the reactivity of sediment transport to hydro-climate change have
103 extensively been highlighted. Neodymium isotopes measured in the silt fractions (Blanchet et
104 al., 2014, 2013, Revel et al., 2015, 2010) of Quaternary sediments have evidenced co-
105 variations of terrigenous flux from the Blue Nile River with monsoon intensity. More
106 recently, (Bastian et al., 2017) have explored the use of Li isotope composition of the clay
107 fractions to determine paleo-variations of silicate weathering in this region. Indeed, lithium
108 isotope composition of river waters and sediments can be used to characterize the weathering
109 intensity (Bouchez et al., 2014, 2013, Dellinger et al., 2017, 2015, 2014; Pogge von
110 Strandmann et al., 2017). Lithium is powerful to trace silicate weathering because it is
111 principally derived from the chemical erosion of silicate minerals (Kisakurek et al., 2005;
112 Millot et al., 2010). During chemical erosion in soils or in weathering profiles, no significant
113 fractionation during rock dissolution can be highlighted (Pistiner and Henderson, 2003; Ryu
114 et al., 2014; Verney-Carron et al., 2011; Wimpenny et al., 2010). In contrast, large isotope
115 fractionations occur during clay neoformation, in favor of the light ${}^6\text{Li}$ (into octahedral sites).
116 At a watershed scale, simple modeling taking into account most recent knowledge on the
117 magnitude of Li isotope fractionation indicate that high clay $\delta^7\text{Li}$ may correspond to low ratio
118 of dissolution/clay neoformation rate (Bastian et al., 2017; Bouchez et al., 2013), or low
119 weathering intensity (Dellinger et al., 2015).

120 A large amount of Li studies is focused on the river dissolved phases (Millot et al., 2010;
121 Pogge von Strandmann et al., 2017; Vigier et al., 2009). However, recently, the potential of

122 river suspended particles (Dellinger et al., 2017, 2015, 2014; Millot et al., 2002), and of
123 sediments deposited in terraces, lake or delta (Bastian et al., 2017; Dosseto et al., 2015) to
124 trace past variations of silicate weathering has also been demonstrated (Bastian et al., 2017;
125 Dosseto et al., 2015; Lechler et al., 2015). By studying the Nile Delta during the last 32kyr,
126 Bastian et al (2017) show that clays deposited by the Nile River were mostly smectite formed
127 in the Ethiopian Traps. Their $\delta^7\text{Li}$ values co-vary with climate proxies, and in particular with
128 precipitation variations. The controls of lithium isotope composition for clays formed in the
129 Ethiopian Traps are therefore important to investigate further, and should help to refine our
130 understanding of the relationships between climate and basalt weathering.

131 In this study, we target to provide chemical erosion rates and related CO_2 consumption rate in
132 the region of the Blue Nile River, the major river draining the Ethiopian Traps basins. For
133 this, we use the first large dataset of chemical compositions of water and particles from most
134 rivers draining the Ethiopian Traps. The objectives are (1) to study weathering rates, their
135 controls, and their relationships with clay Li isotope composition in this region, and (2) to
136 give an estimation of CO_2 consumption rate during an intensive runoff period, well-known
137 and well evidenced in Nile delta sedimentary cores, the African Humid Period (14.5-8kyr).

138

139 **2. Study area**

140

141 The Ethiopian Continental Flood Basalt (CFB) province is located in the North and West
142 Ethiopian highlands (Fig 1 & Fig S1). It covers a surface of about 800,000 km^2 and has an
143 estimated volume ranging between 1 and 1.5 million km^3 (Rochette et al., 1998). They
144 erupted 30 Ma ago over a short time period, 1-2 Ma (Hofmann et al., 1998). The lave pile
145 thickness varies from 500 to 2000 m with maximum thickness of 3000 m in the northern part
146 of the plateau (Mohr. P, 1988). This CFB province is mainly composed by transitional basalts
147 of low-Ti and high-Ti affinities (Pik et al., 1999, 1998), and is covered by a rhyolite terminal
148 formation on the western part of the plateau, along the main escarpment (Ayalew et al., 2002).
149 The Ethiopian Traps exhibits a mean altitude of ~ 3000 m with flat under lying remnants of
150 the original Oligo-Miocene surface. The volcanoes emplaced on the plateau present a higher
151 elevation up to 4600 meters. The Ethiopian Highlands have been uplifted since at least 25 Ma
152 (Pik et al., 2003) with concomitant development of the two main basins of the Nile and
153 Tekeze rivers. The plateau presents important border escarpments with steep slopes,
154 especially along the roughly N-S marginal graben on its Eastern side (Fig. 1). These highlands
155 have been dissected by rapid development and propagation of the Nile and Tekeze basins

156 towards its most and early uplifted Eastern edge (Pik et al., 2003), which acted as the main
157 tectonic drainage divide since Oligo-Miocene times. This tectonic divides is separating the
158 two large westward basins (Nile and Tekeze) from the short and parallel eastward basins
159 developed along the marginal graben after initiation of extension 25 Ma ago (Wolfenden et
160 al., 2004).

161 This tropical region is submitted to the African monsoon, with a mean annual temperature
162 around 21°C. Thus, 90% of the annual precipitations occur during the summer month
163 (Korecha and Barnston, 2007) (Fig 1). Precipitations display an East-West gradient in
164 Ethiopia: rainfall increase from 200 mm/year on the Indian Ocean to 1800 mm/year in the
165 Highlands. At present, the Blue Nile River (major affluent of the Nile River) and its
166 tributaries drain the Ethiopian Traps. Thus, this high topography region is estimated to
167 contribute to 60 % of the total water discharge of the main Nile and to 60 % of its terrigenous
168 sediments (Fielding et al., 2017; Garzanti et al., 2015; Nyssen et al., 2005). In the past, during
169 the last 30 kyr, the positioning and the intensity of the monsoon rain belt has oscillated
170 (Shanahan et al., 2015), in relation with the precession parameter (Tuenter et al., 2003) which
171 lead to stronger precipitation every 21 kyrs. These strong runoff variations are recorded by
172 Ethiopian lake sediments (Amaral et al., 2013) and by the sediments transported by the Nile
173 River and deposited in its delta (Blanchet et al., 2014; Castañeda et al., 2016; Revel et al.,
174 2015, 2010).

175

176 **3. Sampling and methods**

177

178 **3.1. Sampling**

179

180 All samples come from the northern Ethiopian plateau (Fig 1), which encompasses the large
181 catchment of the Blue Nile (64 000 km²), several smaller sub-basins (1000 to 6000 km²), as
182 well as small catchments emplaced directly on the top of the plateau (5 to 100 km²). Two
183 sampling campaigns have been carried out in June 2004 (ETH04) and in March 2005
184 (ETH05). At each sample site, sand, mud and river waters were collected. Waters were
185 filtered on the field with 0.2µm filters and immediately acidified with purified nitric acid.
186 Sands and muds were sampled on the river banks after mixing 5 different aliquots of about
187 100g each. The difference between mud and sand is the visible granulometry: sand samples
188 correspond to coarse sized mineral (> 2mm grain) rich-particles and the mud samples to the

189 finest grain deposits. At the laboratory, clay-size fractions were extracted from the mud
190 samples before chemical and isotope analyses (see section 3.3.2).

191

192 3.2. Runoff Modeling

193

194 The hydrology of the Blue Nile upper basins is strongly controlled by seasonal precipitations,
195 with strong rains and flooding observed during the summer monsoon, from June to September
196 (e.g. Conway, 2009). These conditions are not appropriate for providing a reliable estimate of
197 annual discharge and runoff for each studied zone, using classical methods. In order to
198 provide these estimations for each sampled sub-basin, necessary for weathering rate
199 calculations, we used a numerical model based on the IDRISI © GIS software. This model
200 was run using the plateau topography and available public rainfall data. In order to avoid
201 unconstrained biases linked to evapotranspiration, the output has been convincingly calibrated
202 with current discharge data available for the upper Blue Nile basin (Conway, 1997). These
203 calibrated discharge and runoff data for each sub-basin are presented in Table 1.

204

205 3.3. Analytical protocol

206

207 3.3.1. Chemical analyses

208

209 Major and trace element concentrations were analyzed in waters and sediments using ICP-
210 AES and ICP-MS at the SARM National Facilities in Nancy (France)
211 (<http://helium.crpq.cnrs-nancy.fr/SARM/index.html>). Anions have been measured using ionic
212 chromatography Dionex ICS3000-S with AG11-HC/AS11-HC column. Corresponding
213 uncertainties and detection limits are described in ([http://helium.crpq.cnrs-
214 nancy.fr/SARM/pages/roches.html](http://helium.crpq.cnrs-nancy.fr/SARM/pages/roches.html)).

215

216 3.3.2. Lithium isotope analyses of the clay fractions

217

218 Clays were extracted from the mud samples, by decantation of the sediments in 50ml of ultra-
219 pure water mixed with 20µl of sodium hexametaphosphate (100mg/l). This separation allows
220 to extract particles with a diameter and a density lower than 2 µm and 1.8 respectively. Clay
221 fractions were finely crushed into an agate mortar and 10 mg of the fine powder was
222 mineralized using a concentrated HF/HNO₃/HCl solution in a clean laboratory at LOV, using

223 ultrapure acids. The solution was evaporated and the residue dissolved in 1.00N HCl. The
224 total dissolution of samples was systematically verified by the absence of residue after 20 min
225 of centrifuging at 4000rpm.

226 For major and trace element analyses, an aliquot was diluted 300 times and analyzed by ICP-
227 OES. For lithium isotope analyses, an aliquot containing $\approx 60\text{ng}$ Li was introduced on a
228 cationic resin column and eluted with 1.00N HCl, following the method published in (Bastian
229 et al., 2017; Vigier et al., 2008). This separation was performed twice and allowed Li
230 recovery and purification. For all samples, the total cationic concentration of the sample was
231 constrained to be less than 10% of the total cationic capacity of the column resin. All seawater
232 and rock reference materials were submitted to the exact same protocol.

233 Lithium isotope measurements were performed using a Neptune Plus (ThermoFisher) multi-
234 collector inductively coupled plasma spectrometer (MS-ICP-MS) at the Ecole Nationale
235 Supérieure de Lyon (CNRS National Facilities). Sample was introduced through an Aridus II
236 desolvating system before ionization to increase sensitivity ($1\text{V } ^7\text{Li} / \text{ppb Li}$). We used the jet
237 and X cones, as described in (Balter and Vigier, 2014). To correct for instrumental mass bias,
238 we used the standard bracketing technique, using the LSVEC standard. The total blank
239 procedure is systematically lower than 10pg Li . The accuracy of isotopic analysis was verified
240 by measuring Li7-N reference solution (Carignan et al., 2007) and various reference materials
241 (BE-N basalt, GH granite and seawater). Without chemical purification, an average $\delta^7\text{Li}$ value
242 of $30.2 \pm 0.4\text{‰}$ (2SD, $n=32$) is obtained for the pure Li7-N standard, in agreement with
243 published and theoretical value. After chemical purification, mean $\delta^7\text{Li}$ values are $30.3 \pm 0.4\text{‰}$
244 (2SD, $n=22$), $5.12 \pm 0.9\text{‰}$ (2SD, $n=5$), $1.64 \pm 0.6\text{‰}$ (2SD, $n=3$) and $31.1 \pm 0.6\text{‰}$ (2SD, $n=6$), for
245 Li7-N, BE-N basalt, GH granite and seawater respectively. All values for reference materials
246 compare well with published values (Carignan et al., 2007; Millot et al., 2004).

247

248 **4. Results**

249

250 4.1. Runoff and discharge

251

252 As described in section 3.2, we have estimated runoff values using a specific numerical model
253 including published data for rainfall and discharge, and regional topography. The runoff
254 values determined for 19 sub-basins range from 190 to 273 mm/yr with a mean value of 242
255 mm/yr. The corresponding **calculated** discharges range from $11 \times 10^5 \text{ m}^3/\text{yr}$ (for the Ulet Wenz
256 River) to $1.8 \times 10^{10} \text{ m}^3/\text{yr}$ (for the Blue Nile river), with a mean value of $19 \times 10^8 \text{ m}^3/\text{yr}$ (Table 1).

257 For the Blue Nile river, the calculated discharge is close to the annual discharge measured at
258 the Roseires Dam Station (<http://www.grdc.sr.unh.edu/html/Polygons/P1663800.html>) :
259 4.7×10^{10} m³/yr. The estimated average runoff value of 242 mm/yr for the Ethiopian Traps is in
260 line with the value published in ((Dessert et al., 2003), 129 mm/year). These two comparisons
261 indicate that our model estimates representative values for the runoff and river discharge.
262 The average runoff for this region is two times lower than the estimated value for the Deccan
263 Traps (463 mm/year). It is also lower than the one determined for the Siberian Traps (324
264 mm/yr). Compared to small tropical basaltic areas such as Hawaii (1612 mm/yr) and the
265 Reunion Island (2433 mm/yr), the Ethiopian runoff is also low. This is partly due to their
266 topography, their small surface area compared to the Ethiopian Traps (800,000 km² vs 16760
267 km² in Hawaii and 2512 km² in the Reunion Island), and the occurrence of frequent
268 hurricanes and tropical storms. In Iceland, high runoff (1883-2432 mm/yr) values are mostly
269 due to ice melting, which introduces water in the riverine system during the summer season
270 (Gislason et al., 2009).

271

272 4.2. Major and trace elements

273

274 4.2.1 River waters

275

276 In waters, the dominant cations are, in increasing order of concentrations: Si, Mg, Na, and Ca,
277 with mean values of 447 (\pm 219), 1768 (\pm 502), 712 (\pm 332) and 883 (\pm 417) μ mol/l
278 respectively. These concentrations are corrected from the atmospheric input using Cl
279 concentration and oceanic X/Cl molar ratios, following the method detailed in (Berner and
280 Berner, 1987). After corrections the concentration of Mg*, Na*, and Ca* are 880 (\pm 415), 68
281 (\pm 26) and 574 (\pm 285) μ mol/l respectively.

282 On average, molar Ca*/Na* and Mg*/Na* ratio are 2.5 (\pm 0.9) and 0.4 (\pm 0.6), respectively
283 (Table 2). For comparison, average Ca/Na and Mg/Na in Ethiopian basalts are 3.9 (\pm 1.3) and
284 3.2 (\pm 2.7) respectively, and in the Ethiopian rhyolite are 0.07 (\pm 0.06) and 0.03 (\pm 0.04).

285 When compared with other regions of similar lithologies, river water chemical composition
286 displays roughly a single trend between basalts and rhyolites (Fig. 2). From this trend, it can
287 be estimated that the dissolved contribution coming from rhyolite weathering is low (<15%)
288 compared to basaltic rocks.

289 The dominant anions are, in increasing order of concentrations: HCO₃⁻, SO₄²⁻, Cl⁻, NO₃⁻, and
290 F, with mean values of 3170 (406 to 6039) 202 (15 to 880), 156 (15 to 348), 71 (4 to 292) and

291 10 (5 to 21) $\mu\text{mol/l}$ respectively. The anion concentrations are typical of those measured in
292 other rivers draining basaltic regions (e.g. Dessert et al., 2001).

293

294 4.2.2 River bed particles

295

296 Sands are enriched in SiO_2 compared to mud samples (Table 3), ($51.9 \pm 10.6\%$ on average vs
297 $43.2 \pm 2.6\%$ for muds) and Na_2O ($2.2 \pm 0.8\%$ vs $1.1 \pm 0.5\%$), while depleted in Al_2O_3 (11.7
298 $\pm 3.4\%$ vs $13.0 \pm 3.5\%$ in mud), CaO ($7.0 \pm 3.4\%$ vs $4.7 \pm 2.1\%$ in mud) and Fe_2O_3 ($11.4 \pm$
299 3.4% vs $13.5 \pm 1.5\%$). TiO_2 and MgO ($5.7 \pm 4.0\%$ vs $5.8 \pm 3.1\%$) concentrations are similar
300 between sands and muds: ($\approx 3.1 \pm 1.4\text{ wt}\%$ and $\approx 5.8 \pm 3.1\text{ wt}\%$ respectively). Si/Al ratio is
301 lower by $\approx 30\%$ in muds compared to sands, which is consistent with occurrence of
302 aluminosilicate minerals (clays/smectite) in the collected muds. The chemical composition of
303 $<2\mu\text{m}$ clay fractions extracted from mud samples, contains, on average, 24.2% ($\pm 4.7\%$)
304 Al_2O_3 , 22.2% ($\pm 1.8\%$) Fe_2O_3 , and 15.1% ($\pm 6.9\%$) MgO . We note that the mud samples
305 collected in river banks are not representative of the clay fraction separated at the laboratory
306 and rather reflects a mixing between clays and primary phases. Thus, clay fractions ($<2\mu\text{m}$)
307 were preferentially used for assessing weathering processes in this region.

308 Some trace elements measured in the solid phases can be used to study chemical erosion
309 degree or intensity (Louvat and Allègre, 1997; P Louvat and Allègre, 1998). In the diagram
310 Sr/Th versus U/Th (Fig 3, Table 2 and 3), when compared to bedrocks, Ethiopian river waters
311 display elevated U/Th and Sr/Th ratios (respectively >2 and > 8405) while the solid phases
312 display low U/Th and Sr/Th values (respectively <0.3 and <87.8). Sr and U are two mobile
313 elements during water-rock interactions and are usually depleted in the solid phase, in contrast
314 with Th, which is an immobile element that can easily adsorb, except in organic-rich
315 environments (Dupré et al., 1999). Figure 3 also indicates that the river particles are mostly
316 derived from basaltic rocks, as previously described, and that the influence from rhyolite
317 weathering is minimal, except for one sample (Nazero Wenz), which is located in a rhyolite
318 rich area (Figure S1).

319

320 4.3 Lithium isotope compositions of clay size ($<2\mu\text{m}$) fractions

321

322 Ethiopian bedrock samples exhibit a mean $\delta^7\text{Li}$ value of $5 \pm 0.5\text{‰}$ ($n=3$) (Bastian et al., 2017)
323 (Fig. 4), which compares well with the range published for intraplate basalts. Compared to
324 these rocks, or to tholeiitic basalts (3.1 to 5.2‰ , (Elliott et al., 2006)), and to OIB basalts (3.1

325 - 5.2 ‰, (Genske et al., 2014)) clays deposited by Ethiopian rivers are significantly enriched
326 in ⁶Li: clay δ⁷Li values range from 0.3‰ (± 0.5‰) to 4‰ (± 0.5‰), with a mean value of
327 2.0‰ (± 1.2‰). This is consistent with preferential enrichment in light lithium isotope during
328 smectite neoformation, as seen experimentally (Vigier et al., 2008) and in basaltic soils (Huh
329 et al., 2004; Kisakürek et al., 2004; Pistiner and Henderson, 2003; Ryu et al., 2014).
330 In the literature, a large range of δ⁷Li values is observed in suspended particles (SPM) of
331 rivers draining basaltic regions e.g. in Iceland (with values from -1.3 to 7.5‰, (von
332 Strandmann et al., 2006)) and in the Azores archipelago (3.5 to 9.5‰, (von Strandmann et al.,
333 2010)). Also in soils, the range of published δ⁷Li for bulk soils samples is large (-15 to 10‰,
334 (Clergue et al., 2015; Pistiner and Henderson, 2003; Ryu et al., 2014; Schmitt et al., 2012; von
335 Strandmann et al., 2012)). These observed variations are possibly due to mixing between clay
336 and primary minerals, because these samples are not necessarily representative of clay pure
337 endmember (Dellinger et al., 2014). Here, clays were extracted from river sediments in order
338 to minimize the influence of primary minerals.

339

340 **5. Discussion**

341

342 **5.1. Assessing weathering processes at the basin scale**

343

344 As described in section 4.2, chemical and isotopic compositions of river waters and particles
345 can give indications on weathering rates and/or intensity at the watershed scale. Some
346 elements are particularly mobile during basalt alteration (e.g. Sr, K, Na), and preferentially
347 lost from weathering profiles after a short period of time (Chadwick et al., 1999; Ryu et al.,
348 2014). Thus, as described in section 4.2, Sr and U are depleted in sands and mud samples,
349 while enriched into the dissolved phases (Fig. 2) of the corresponding rivers. Also, Na, Ca and
350 Mg concentrations are typical of waters draining basaltic rocks (Fig. 3). However, using
351 elementary ratios, or elementary concentrations, it is often difficult to distinguish the role of
352 lithology from the one of dissolution or leaching process, because of the chemical diversity of
353 the drained bedrocks. As described in previous works (Pistiner and Henderson, 2003; Vigier
354 et al., 2008; Wimpenny et al., 2010), lithium isotopes provide a complementary mean to
355 examine chemical erosion processes (Bastian et al., 2017; Dellinger et al., 2015). Bastian et
356 al., (2017), have analyzed 55 clay fractions extracted from Nile deep sea fan core sediments.
357 Their δ⁷Li values vary between 4 and -1.2 ‰ during the last 32,000 years. In their study, clay
358 δ⁷Li were related to the ratio between dissolved Li flux and the flux of Li incorporated in the

359 secondary phases (F_{lea}^{Li}/F_{sp}^{Li}). In rivers currently draining the Ethiopian Traps, clay fractions
 360 display variable $\delta^7\text{Li}$ values, from 0.3‰ to 4.0‰, a range that is similar to the 0-32 kyr clays
 361 deposited in the Nile delta. Clay $\delta^7\text{Li}$ and Mg/Ti ratios display a positive correlation (shown
 362 in fig. 4), which suggests that both proxies are impacted by similar processes during basalt
 363 weathering. This is not surprising since Li^+ essentially substitutes to Mg^{2+} during smectite
 364 formation (Decarreau et al., 2012; Vigier et al., 2008), and smectite is the most abundant
 365 phase carried by rivers draining the Ethiopian Traps (Garzanti et al., 2015).

366 Using a simple modeling, based on mass balance, clay $\delta^7\text{Li}$ values have been shown to be
 367 essentially explained by the ratio of leaching versus clay formation rates, and thus reflect
 368 different weathering intensities (Bastian et al., 2017; Bouchez et al., 2013; Vigier et al., 2009;
 369 Vigier and Godd ris, 2015; von Strandmann et al., 2012). The behavior of Li isotopes at the
 370 scale of a watershed or of a continent has been described with the following equations,
 371 considering a simple mass balance between bedrock, rivers and soils at the watershed scale. It
 372 is defined such that all the lithium released by rock dissolution is either incorporated into
 373 secondary phases formed in weathering profiles or released into superficial waters (and *in fine*
 374 in rivers).

375

$$376 \quad F_{lea}^{Li}\delta_{lea} = F_{sp}^{Li}\delta_{sp} + F_{riv}^{Li}\delta_{riv} \quad \text{equation (1)}$$

377

378 where F_{lea}^{Li} , F_{sp}^{Li} , and F_{riv}^{Li} are the Li flux related to dissolution, secondary phase precipitation
 379 and soil water outflow respectively. δ_{lea} , δ_{sp} , δ_{riv} are the Li isotopic signature ($\delta^7\text{Li}$ value) of
 380 the dissolved phase, the secondary phase, the river water and the bedrock, respectively. Since
 381 basalt dissolution is isotopically congruent, $\delta_{lea} = \delta_{Bedrock}$ (Verney-Carron et al., 2011;
 382 Wimpenny et al., 2010). The isotope fractionation between dissolved phase and the secondary
 383 phases is noted Δ_{land} . After simplification, the isotope composition of the secondary phases is
 384 given by:

385

$$386 \quad \delta_{sp} = \frac{\Delta_{land}}{F_{lea}^{Li}/F_{sp}^{Li}} + \delta_{BedRock} - \Delta_{land} \quad \text{Equation (2)}$$

387

388 This equation states that if F_{sp}^{Li} is close to F_{lea}^{Li} , then $\delta_{sp} = \delta_{BedRock}$. If F_{sp}^{Li} is low compared
 389 to F_{lea}^{Li} , then $\delta_{sp} = \Delta_{land}$.

390

391 The positive correlation between clay $\delta^7\text{Li}$ and Mg/Ti cannot be explained by a binary mixing
392 between bedrocks and Li-rich clays, as illustrated in Figure 4. Thus, a similar mass balance
393 between rocks and weathering products, as for $\delta^7\text{Li}$, was applied to clay Mg/Ti . For solving it,
394 we assumed that no Ti is released into water during dissolution (due to the high immobility of
395 this element during water/rock interactions) ($\text{Ti}_{rlea} = 0$). Thus Mg/Ti ratio of secondary
396 phases can be described as:

397

$$398 \quad \left(\frac{\text{Mg}}{\text{Ti}}\right)_{sp} = \frac{1}{\frac{F_{lea}^{\text{Mg}}}{F_{sp}^{\text{Mg}}} \cdot \frac{\text{Ti}_{clay}^{mean}}{\text{Mg}_{BedRock}}} \quad \text{Equation (3)}$$

399

400 The relation between the Li and the Mg flux becomes:

401

$$402 \quad \frac{F_{lea}^{\text{Li}}}{F_{sp}^{\text{Li}}} \cdot \beta = \frac{F_{lea}^{\text{Mg}}}{F_{sp}^{\text{Mg}}} \quad \text{Equation (4)}$$

403 with β reflecting the Li/Mg ratio of the clay fraction (normalized to the source rock one).

404 As shown in Figure 4, some basins are characterized by low clay $\delta^7\text{Li}$ and low Mg/Ti values,
405 (ie Jara Wenz (ETH05-11), Borkena Wenz (ETH05-13), Robi Wenz (ETH05-4), Meri Wenz
406 (ETH05-28), Tikur Wenz (ETH05-19)). For these small basins, the weathering model
407 indicates that soil formation rate (F_{sp}) is low compared to the leaching rate (F_{lea}). Other areas
408 display high clay $\delta^7\text{Li}$ values associated to high Mg/Ti ratios (Ketching Abeba Wenz
409 (ETH05-25), Gereb Ara Wenz (ETH05-40), Tekeze (ETH0535), Hormat Wenz (ETH05-47),
410 Ala-Wiha (ETH05-20), Nazero Wenz (ETH05-6)).

411 Following our modeling, the various $\delta^7\text{Li}$ and Mg/Ti values are best explained by variations
412 of the weathering intensity, leading also to a large range of clay Li/Mg (β parameter). For a
413 large part, the β values are greater than 1 (Fig. 4). This indicates that Li is more retained in the
414 weathering profiles than Mg (compared to source rocks). This is consistent with observations
415 made in various Hawaiian weathering profiles where kaolinite prevail (Ryu et al., 2014).

416 Thus, the trend between clay $\delta^7\text{Li}$ and clay Mg/Ti is likely due to variable weathering
417 conditions. However, no clear relationship with the runoff, the topography or vegetation can
418 be highlighted for this group of rivers. Since Mg is involved in the vegetation cycle, and Li is
419 not, perhaps a loss of Mg in relation with recent plant and root activity can also explain part of

420 this variability. More work would certainly need to be undertaken in the most vegetated areas
421 of this region since no convincing correlation between $\delta^7\text{Li}$ or Mg/Ti and physical parameters
422 such as the slope, runoff, vegetation and land use can be highlighted here. This suggests that,
423 at present, basalt weathering and soil production rate in the Blue Nile Basin are variable in
424 space, and that this variation is likely to be a complex function of several parameters.

425

426 **5.2. Weathering rates and controls in the Upper Blue Nile Basin**

427

428 As discussed above, the relatively large range of clay Mg/Ti and $\delta^7\text{Li}$ reflects a significant
429 variation of weathering conditions in the Ethiopian Traps region while the lithology is
430 dominantly basaltic. It is possible to use the chemical composition of river waters in order to
431 quantify present-day weathering rates (Table 2) at the scale of each corresponding watershed
432 (e.g. Gaillardet et al., 1999; Stallard and Edmond, 1983). The Total Dissolved Solid (TDS) is
433 defined by the sum of major mobile cations (Ca, Mg, K and Na) concentrations in the
434 dissolved phases of rivers. These concentrations are corrected from the atmospheric input
435 using Cl concentration and oceanic X/Cl molar ratios, following the method detailed in (Das
436 et al., 2005). TDS* values (* indicate corrected from atmospheric inputs) estimated from
437 concentrations measurement in the dissolved phase of the Blue Nile Basin rivers range from
438 9.5 to 111.0 mg/l, with a mean value of 67 mg/l. In the diagram TDS* versus temperature, the
439 Blue Nile tributaries plot along the same trend defined by all other basaltic regions studied
440 thus far (Fig. 5a). This first indicates the good representative nature of our sampling and
441 methods. The average TDS* for the Ethiopian Traps is as high as the one determined for the
442 Deccan Traps (54 mg/l) and for Java Island (43 mg/l) (Dessert et al., 2003; Li et al., 2016),
443 which are also characterized by elevated annual temperature (27°C and 24.8 °C respectively).
444 These three regions display river TDS* values significantly greater than in Hawaii (7.4 mg/l)
445 and in Iceland (8.8-10.3 mg/l), displaying both lower surface temperatures on average (16 and
446 2 °C respectively). This trend confirms that, for basaltic basins, temperature is a key
447 parameter which controls river TDS* (Dessert et al., 2003; Li et al., 2016).

448 Using the TDS* values, the estimated annual discharge, and the watershed area, it is possible
449 to determine silicate weathering rates. These rates in the Ethiopian Traps basins range from
450 2.6 to 24.4 tons/km²/year, with a mean value of 16.1 tons/km²/year (Table 2). For the Blue
451 Nile River, sampled at the output of the Ethiopian Traps (see map Fig. 1), the silicate
452 weathering rate is 11.3 tons/km²/year. The mean value estimated for chemical erosion rate in
453 the Ethiopian Traps, based on 17 data (Table 2), is consistent with the positive correlation

454 previously observed with the runoff (see Fig. 5b, (Dessert et al., 2003)). In contrast to TDS*,
455 weathering rates in Ethiopia are low compared to other regions of similar lithology. For
456 instance, the weathering rate in the Deccan Traps is 25.1 tons/km²/year, 48.4 tons/km²/year
457 for La Reunion, and 152 tons/km²/year for Java (Dessert et al., 2003). Lower runoff in the
458 Ethiopian Traps (242 mm/years) compared to these regions is certainly a key factor. However,
459 other parameters may also play a role, in particular temperatures, the age of the basaltic rocks
460 (Li et al., 2016), the soil age (Ryu et al., 2014; Vigier et al., 2005), and formation of glassy
461 material in volcanically active area (e.g. Java Island and Iceland) (Gislason et al., 2009;
462 Gislason and Oelkers, 2003; Vigier et al., 2009).

463 Overall, both river particles and water composition can provide valuable information on
464 chemical erosion rate in the various basins. However here there is no correlation between
465 river particles and water chemical compositions. This is likely to be due to a recent
466 decoupling between soil (or weathering profile) formation and river aqueous phase. Indeed,
467 large soil reservoir where clays have formed can encompass different weathering conditions,
468 issued from past climate variations, and may therefore not be representative of the current
469 state. Recent observations in the Nile deltaic sediments show that both chemical and physical
470 erosion responded rapidly to hydro-climate change in the last 30kyr (Bastian et al., 2017).
471 This argues for a residence time of clay-rich sediments that is not above a few thousand years
472 at most, in coherence with elevated topography of the Traps where clays mainly come from.
473 The observed decoupling between clays and waters must then have occurred just recently,
474 perhaps due to intensification of anthropic activities in this region (Lanckriet et al., 2015)

475

476 **5.3. CO₂ consumption and SO₄²⁻ concentration due to silicate weathering**

477

478 From river water chemical compositions, it is possible to estimate the CO₂ consumption rates
479 related to silicate weathering. In the literature, several methods have been used, using
480 corrections from source rocks in mixed lithology basins, calcium concentration in silicate
481 rivers (Goddéris et al., 2013), or HCO₃⁻ concentrations in carbonate-free watersheds (e.g. Das
482 et al., 2005). Since the Ethiopian Traps are essentially constituted of silicate rocks, with little
483 vegetated areas, major cations concentrations in rivers have only been corrected for
484 atmospheric inputs, as described in section 5.1. HCO₃⁻ concentrations are determined using
485 the following electronic mass balance:

486

$$487 \quad [\text{HCO}_3^-] = 2[\text{Ca}^{2+}] + [\text{K}^+] + 2[\text{Mg}^{2+}] - 2[\text{SO}_4^{2-}] - [\text{F}^-] - [\text{NO}_3^-] \text{ Equation (5)}$$

488

489 where all concentrations are corrected for atmospheric inputs (see section 4.2.1). The average
490 pH of the Ethiopian rivers (7.5-8.2, (MERID, 2005)) makes it possible to assume that
491 HCO_3^- is the dominant anion compared to CO_3^{2-} . Thus, in order to determine the CO_2
492 consumption related to silicate weathering, we consider that 1 mole of HCO_3^- exported by
493 rivers corresponds to 1 mole of consumed atmospheric CO_2 . CO_2 consumption rates are then
494 calculated using the river discharge and the basin surface area (for specific rates). Some recent
495 studies (Calmels et al., 2007; Li et al., 2008; Torres et al., 2016) show that sulfate mineral
496 dissolution produces sulfuric acid that can enhance bedrock and mineral dissolution, in
497 particular in sedimentary or carbonate rich context. Any silicate weathering due to sulfuric
498 acid may lead to an overestimation of the CO_2 consumption rate if this effect is not considered
499 into the calculations. In the rivers studied here, dissolved sulfate concentrations do not
500 correlate to dissolved nitrate but rather with elements that are mobile during silicate
501 dissolution (for example Ca and Mg). This suggests that sulfates are not significantly related
502 to fertilizer addition but may mostly derive from weathering and oxidizing processes. This is
503 not surprising since this region is not intensively cultivated, and is also supported by small
504 amounts of nitrate in waters (see section 4.2.1). The use of Equation (5) to calculate HCO_3^-
505 allows us to avoid a potential bias due to sulfuric acid in the determination of CO_2
506 consumption rate.

507 Table 2 show that specific CO_2 consumption rate due to basalt dissolution in Ethiopian Traps
508 vary from 0.11×10^6 mol/km²/yr (for the Ulet-Wenz basin) to 1.33×10^6 mol/km²/yr (for the
509 Ketchiin Abeba Wenz), and is 0.76×10^6 mol/km²/yr on average. The CO_2 consumption rate
510 cover a large range, possible due to local – small scale - effects. Thus, for the comparison
511 with literature data, we use the two values estimated for the Blue Nile River, which integrates
512 most waters draining the Ethiopian Traps. The Blue Nile River was sampled at two different
513 seasons (ETH04-2; Juin-04 and ETH05-52; Mars -05). The two samples lead to similar CO_2
514 consumption rate, of 0.49 and 0.52 mol/km²/yr respectively, but are low compared to other
515 basaltic regions. For comparison, this flux is estimated to be 1.26×10^6 mol/km²/yr for the
516 Deccan Traps and 6.41×10^6 mol/km²/yr for Java Island (Dessert et al., 2003). The CO_2
517 consumption rate due to silicate weathering in the Blue Nile basin is slightly higher, than the
518 value published by (Dessert et al., 2003) for the Ethiopian Traps, i.e. 0.15×10^6 mol/km²/yr.
519 When using the Dessert et al., (2003) theoretical equation $f\text{CO}_2 = R_f \times 323.44 \exp(0.0642 T)$
520 where $f\text{CO}_2$, R_f and T are respectively the specific atmospheric CO_2 consumption

521 (mol/km²/year), the runoff (mm/year) and the temperature (°C), the corresponding
522 consumption rate is also slightly lower (0.16x10⁶ mol/km²/year) than our calculated value.

523 In order to determine the relative role of the Blue Nile Basin in the present-day carbon cycle,
524 one needs to estimate its total CO₂ consumption flux (in mol/year). The average CO₂
525 consumption rate is calculated to be 0.65x10¹² mol/year. This is significantly higher than in
526 Iceland (0.070 x10¹² mol/year), the Reunion Island (0.006 x10¹² mol/year) or the Azores
527 (0.0004 x10¹² mol/year) (see Fig. 6). However, this value remains lower than for the Deccan
528 (0.392 x10¹² mol/year) or than SE Asia (1.033 x10¹² mol/year). The upper Blue Nile represent
529 a CO₂ consumption close to the global average ((Gaillardet et al., 1999), see Fig. 6), and only
530 7.5 % of the total CO₂ consumed by silicate weathering on Earth. It corresponds to 7.8.10³Gt
531 of carbon consumed by year, which is the equivalent of 0.4% of the total human carbon
532 emission per year. Our results demonstrate that, at present, the Ethiopian Traps weathering
533 has a negligible impact on the carbon cycle, and thus on global climate.

534 In the past, this could however be different. First, as described in the Introduction, the
535 modeling study from Lefebvre et al., (2013), show that, during the Oligocene, the Ethiopian
536 Traps was likely the most important region on Earth in terms of silicate weathering. More
537 recently, since 100kyr, the North East African region is known to have been submitted to
538 extreme variations of precipitation and runoff. The monsoon rain belt oscillated together with
539 the precession cycle of 21,000 years. This induced succession of “humid” and “arid” periods
540 that affected sediment flux and physical erosion in this region. This is evidenced in lakes
541 where arid periods are characterized by hiatus or paleo-soils in the sedimentary records and
542 water level variations (for lake Turkana, lake Abhé (Forman et al., 2014; Garcin et al., 2009;
543 Hoelzmann et al., 2010)). This is also observed in the marine cores of the Nile deep-sea-fan,
544 with much higher sedimentation rates during humid periods (Revel et al., 2015, 2014, 2010).

545 Based on both observations and modeling, it is possible to provide first extrapolation of our
546 results to some critical period of the Quaternary period. Indeed, recent studies illustrate that
547 during this time, silicate weathering rates were able to respond rapidly to climate change
548 (Bastian et al., 2017; Dosseto et al., 2015; Rothacker et al., 2018). This region was submitted
549 to large changes of the African Monsoon intensity (Shanahan et al., 2015) while runoff likely
550 plays a key role on basalt weathering and related CO₂ consumption ((Goddéris et al., 2013),
551 see also Fig. 5b and 8). Since 6 kyr, the climate in the Ethiopian Traps is characterized by
552 relatively low monsoonal precipitation and low runoff. However, between 15 and 8 kyr,
553 during the African Humid Period (AHP), this region was submitted to much higher
554 precipitation rates (Blanchet et al., 2013; Revel et al., 2014). Climate modeling studies, using

555 LMDZ and ORCHIDEE models, determined an increase of precipitation in the Ethiopian
556 Traps of 1.4 to 2.5 times larger during the AHP ((Marzin and Braconnot, 2009) ; Vadsaria and
557 Ramstein, Pers. Comm.). This corresponds to a runoff ranging between 340 and 600
558 mm/years. By applying this factor, CO₂ consumption rate during African Humid Period may
559 thus have increased up to values of 0.91-1.5x10¹² mol/yr (brown bar in Fig. 6), which
560 corresponds to the most elevated current rates. These estimations are in line with the study of
561 (Lefebvre 2013), which showed that the importance of this region in the carbon cycle during
562 the Oligocene period. However, it is important to note that during the Oligocene, the global
563 temperature was also higher, while for the AHP, the runoff increase in North Africa is likely
564 not related to a significant increase of temperature (De Boer et al., 2013).
565 These results also suggest a potential increase of global CO₂ consumption during more humid
566 periods due to increase of silicate weathering. Indeed, other large basaltic regions (e.g.
567 Deccan, Parana) are also located in the tropical zone influenced by monsoon. This is likely a
568 key for understanding past rapid climate change and the influence of tropical basins on the
569 carbon cycle.

570

571 **6. Conclusion**

572

573 This study examines the chemical composition of river water and sediments in the Ethiopian
574 Traps in order to characterize silicate weathering and corresponding CO₂ consumption in this
575 region. Lithium isotopic composition of the clay fractions was also examining and present a
576 positive correlation with clay Mg/Ti ratios, in relation with variable weathering conditions in
577 this region.

578 The average weathering rate (16.1 tons/km²/yr) and CO₂ consumption rate (0.65.10¹² mol/yr)
579 determined for the Ethiopian Traps are lower than for other basaltic regions (e.g. Deccan or
580 SE Asia). This is bet explained by the low runoff values observed in Ethiopia at present (242
581 mm/yr), despite regular occurrence of the monsoon. This demonstrates that, at present, the
582 Ethiopian Traps weathering has a negligible impact on the carbon cycle, and thus on climate.

583 In the recent or the remote past, such as during the African Humid Period (from 14.500 to
584 8.000 years BP) or during the Oligocene (30 Ma) when this region was under equatorial
585 latitudes, the runoff was increased to much higher values that modelers have estimated. Based
586 on these results and weathering models, we find comparable results for CO₂ consumption rate
587 for both periods. The determined CO₂ consumption rate for the African Humid Period range

588 between 0.91 and $1.5 \cdot 10^{12}$ mol/yr. This indicates that during humid periods the Ethiopian
589 traps could have played a significant role on carbon cycle and on climate.

590 Overall, this study brings out the key role of a region that is understudied thus far in terms of
591 weathering and climate paleo-variations. More generally, the influence on global climate of
592 tropical basins influenced by monsoon would deserve to be assessed more precisely, in
593 particular those of basaltic lithology.

594

595

596

597 **Acknowledgments**

598

599 This work was supported by BQR Geoazur, CNRS INSU-SYSTER grants and ANR
600 INTOCC. We thank P. Telouk (LGLTPE) for his assistance with the ENS-Lyon Neptune
601 *plus*. We thank also P.H Blard and B. Marty (CRPG) for their help on the field and fruitful
602 discussions.

603

604 **References**

605

- 606 Amaral, P.G.C., Vincens, A., Guiot, J., Buchet, G., Deschamps, P., Doumnang, J.C.,
607 Sylvestre, F., 2013. Palynological evidence for gradual vegetation and climate changes
608 during the African Humid Period termination at 13°N from a Mega-Lake Chad
609 sedimentary sequence. *Clim. Past* 9, 223–241. <https://doi.org/10.5194/cp-9-223-2013>
- 610 Ayalew, D., Barbey, P., Marty, B., Reisberg, L., Yirgu, G., Pik, R., 2002. Source, genesis, and
611 timing of giant ignimbrite deposits associated with Ethiopian continental flood basalts.
612 *Geochim. Cosmochim. Acta* 66, 1429–1448. [https://doi.org/10.1016/S0016-](https://doi.org/10.1016/S0016-7037(01)00834-1)
613 [7037\(01\)00834-1](https://doi.org/10.1016/S0016-7037(01)00834-1)
- 614 Balter, V., Vigier, N., 2014. Natural variations of lithium isotopes in a mammalian model.
615 *Metallomics* 6, 582. <https://doi.org/10.1039/c3mt00295k>
- 616 Bastian, L., 2017. Thèse de doctorat Bastian Luc Impact des variations de la mousson
617 Africaine sur l' érosion chimique des silicates dans le bassin versant du Nil depuis.
- 618 Bastian, L., Revel, M., Bayon, G., Dufour, A., Vigier, N., 2017. Abrupt response of chemical
619 weathering to Late Quaternary hydroclimate changes in northeast Africa. *Sci. Rep.* 7,
620 44231. <https://doi.org/10.1038/srep44231>
- 621 Bayon, G., Dennielou, B., Etoubleau, J., Ponzevera, E., Toucanne, S., Bermell, S., 2012. Use
622 in Iron Age Central Africa. *Science* (80-.). 335, 1219–1222.
623 <https://doi.org/10.1126/science.1215400>
- 624 Bayon, G., Skonieczny, C., Delvigne, C., Toucanne, S., Bermell, S., Ponzevera, E., André, L.,
625 2016. Environmental Hf-Nd isotopic decoupling in World river clays. *Earth Planet. Sci.*
626 *Lett.* 438, 25–36. <https://doi.org/10.1016/j.epsl.2016.01.010>
- 627 Benedetti, M.F., Menard, O., Noack, Y., Carvalho, A., Nahon, D., 1994. Water-rock
628 interactions in tropical catchments: field rates of weathering and biomass impact. *Chem.*
629 *Geol.* 118, 203–220. [https://doi.org/10.1016/0009-2541\(94\)90177-5](https://doi.org/10.1016/0009-2541(94)90177-5)
- 630 Berner, E., Berner, R.A., 1987. *The Global Water Cycle. Geochemistry Environ.* Prentice
631 Hall.
- 632 Blanchet, C.L., Frank, M., Schouten, S., 2014. Asynchronous changes in vegetation, runoff
633 and Erosion in the Nile River watershed during the Holocene. *PLoS One* 9, 1–18.
634 <https://doi.org/10.1371/journal.pone.0115958>
- 635 Blanchet, C.L., Tjallingii, R., Frank, M., Lorenzen, J., Reitz, A., Brown, K., Feseker, T.,
636 Brückmann, W., 2013. High- and low-latitude forcing of the Nile River regime during
637 the Holocene inferred from laminated sediments of the Nile deep-sea fan. *Earth Planet.*
638 *Sci. Lett.* 364, 98–110. <https://doi.org/10.1016/j.epsl.2013.01.009>
- 639 Bouchez, J., Gaillardet, J., von Blanckenburg, F., 2014. Weathering Intensity in Lowland
640 River Basins: From the Andes to the Amazon Mouth. *Procedia Earth Planet. Sci.* 10,
641 280–286. <https://doi.org/10.1016/j.proeps.2014.08.063>
- 642 Bouchez, J., Von Blanckenburg, F., Schuessler, J.A., 2013. Modeling novel stable isotope
643 ratios in the weathering zone. *Am. J. Sci.* 313, 267–308.
644 <https://doi.org/10.2475/04.2013.01>
- 645 Brady, P. V, Carroll, S.A., 1994. Direct effects of CO₂ and temperature on silicate

646 weathering: Possible implications for climate control. Pergamon *Geochimica*
647 *Cosmochim. Acta* 58, 1853–1856. [https://doi.org/10.1016/0016-7037\(94\)90543-6](https://doi.org/10.1016/0016-7037(94)90543-6)

648 Brady, P. V, Dorn, R.I., Brazel, A.J., Clark, J., Moore, R.B., Glidewell, T., 1999. Direct
649 measurement of the combined effects of lichen, rainfall, and temperature on silicate
650 weathering. *Geochim. Cosmochim. Acta* 63, 3293–3300. [https://doi.org/10.1016/S0016-](https://doi.org/10.1016/S0016-7037(99)00251-3)
651 [7037\(99\)00251-3](https://doi.org/10.1016/S0016-7037(99)00251-3)

652 Calmels, D., Gaillardet, J., Brenot, A., France-Lanord, C., 2007. Sustained sulfide oxidation
653 by physical erosion processes in the Mackenzie River basin: Climatic perspectives.
654 *Geology* 35, 1003–1006. <https://doi.org/10.1130/G24132A.1>

655 Carignan, J., Vigier, N., Millot, R., 2007. Three secondary reference materials for lithium
656 isotope measurements: Li7-N, Li6-N and LiCl-N solutions. *Geostand. Geoanalytical Res.*
657 31, 7–12. <https://doi.org/10.1111/j.1751-908X.2007.00833.x>

658 Castañeda, I.S., Schouten, S., Pätzold, J., Lucassen, F., Kasemann, S., Kuhlmann, H.,
659 Schefuß, E., 2016. Hydroclimate variability in the Nile River Basin during the past
660 28,000 years. *Earth Planet. Sci. Lett.* 438, 47–56.
661 <https://doi.org/10.1016/j.epsl.2015.12.014>

662 Chadwick, O.A., Derry, L.A., Vitousek, P.M., Huebert, B.J., Hedin, L.O., 1999. Changing
663 sources of nutrients during four million years of ecosystem development Terrestrial
664 biogeochemists traditionally distinguish atmospherically derived from rock-derived
665 elements. *Nat. www.nature.com* 397.

666 Clergue, C., Dellinger, M., Buss, H.L., Gaillardet, J., Benedetti, M.F., Dessert, C., 2015.
667 Influence of atmospheric deposits and secondary minerals on Li isotopes budget in a
668 highly weathered catchment, Guadeloupe (Lesser Antilles). *Chem. Geol.* 414, 28–41.
669 <https://doi.org/10.1016/j.chemgeo.2015.08.015>

670 Conway, D., 1997. A water balance model of the Upper Blue Nile in Ethiopia. *Hydrol. Sci. J.*
671 42, 265–286. <https://doi.org/10.1080/02626669709492024>

672 Das, A., Krishnaswami, S., Sarin, M.M., Pande, K., 2005. Chemical weathering in the
673 Krishna Basin and Western Ghats of the Deccan Traps, India: Rates of basalt weathering
674 and their controls. *Geochim. Cosmochim. Acta* 69, 2067–2084.
675 <https://doi.org/10.1016/j.gca.2004.10.014>

676 De Boer, E.J., Hooghiemstra, H., Vincent Florens, F.B., Baider, C., Engels, S., Dakos, V.,
677 Blaauw, M., Bennett, K.D., 2013. Rapid succession of plant associations on the small
678 ocean island of Mauritius at the onset of the Holocene. *Quat. Sci. Rev.* 68, 114–125.
679 <https://doi.org/10.1016/j.quascirev.2013.02.005>

680 Decarreau, A., Vigier, N., Pálková, H., Petit, S., Vieillard, P., Fontaine, C., 2012. Partitioning
681 of lithium between smectite and solution: An experimental approach. *Geochim.*
682 *Cosmochim. Acta* 85, 314–325. <https://doi.org/10.1016/j.gca.2012.02.018>

683 Dellinger, M., Bouchez, J., Gaillardet, J., Faure, L., Moureau, J., 2017. Tracing weathering
684 regimes using the lithium isotope composition of detrital sediments. *Geology* 45, 411–
685 414. <https://doi.org/10.1130/G38671.1>

686 Dellinger, M., Gaillardet, J., Bouchez, J., Calmels, D., Louvat, P., Dosseto, A., Gorge, C.,
687 Alanoca, L., Maurice, L., 2015. Riverine Li isotope fractionation in the Amazon River
688 basin controlled by the weathering regimes. *Geochim. Cosmochim. Acta* 164, 71–93.

- 689 <https://doi.org/10.1016/j.gca.2015.04.042>
- 690 Dellinger, M., Gaillardet, J.Ô., Bouchez, J., Calmels, D., Galy, V., Hilton, R.G., Louvat, P.,
691 France-Lanord, C., 2014. Lithium isotopes in large rivers reveal the cannibalistic nature
692 of modern continental weathering and erosion. *Earth Planet. Sci. Lett.* 401, 359–372.
693 <https://doi.org/10.1016/j.epsl.2014.05.061>
- 694 Dessert, C., Dupre, B., Francois, L.M., Schott, J., Gaillardet, J., Chakrapani, G., Bajpai, S.,
695 2001. Erosion of Deccan Traps determined by river geochemistry; impact on the global
696 climate and the (super 87) Sr/ (super 86) Sr ratio of seawater. *Earth Planet. Sci. Lett.* 188,
697 459–474.
- 698 Dessert, C., Dupré, B., Gaillardet, J., François, L.M., Allègre, C.J., 2003. Basalt weathering
699 laws and the impact of basalt weathering on the global carbon cycle. *Chem. Geol.* 202,
700 257–273. <https://doi.org/10.1016/j.chemgeo.2002.10.001>
- 701 Dosseto, A., Vigier, N., Joannes-Boyau, R., Moffat, I., Singh, T., Srivastava, P., 2015. Rapid
702 response of silicate weathering rates to climate change in the Himalaya. *Geochemical
703 Perspect. Lett.* 10–19. <https://doi.org/10.7185/geochemlet.1502>
- 704 Dupré, B., Viers, J., Dandurand, J.L., Polve, M., Bénézech, P., Vervier, P., Braun, J.J., 1999.
705 Major and trace elements associated with colloids in organic-rich river waters:
706 Ultrafiltration of natural and spiked solutions. *Chem. Geol.* 160, 63–80.
707 [https://doi.org/10.1016/S0009-2541\(99\)00060-1](https://doi.org/10.1016/S0009-2541(99)00060-1)
- 708 Elliott, T., Thomas, A., Jeffcoate, A., Niu, Y., 2006. Lithium isotope evidence for subduction-
709 enriched mantle in the source of mid-ocean-ridge basalts. *Nature* 443, 565–568.
710 <https://doi.org/10.1038/nature05144>
- 711 Fielding, L., Najman, Y., Millar, I., Butterworth, P., Ando, S., Padoan, M., Barfod, D.,
712 Kneller, B., 2017. A detrital record of the Nile River and its catchment. *J. Geol. Soc.
713 London.* 174, 301–317. <https://doi.org/10.1144/jgs2016-075>
- 714 Forman, S.L., Wright, D.K., Bloszies, C., 2014. Variations in water level for Lake Turkana in
715 the past 8500 years near Mt. Porr, Kenya and the transition from the African Humid
716 Period to Holocene aridity. *Quat. Sci. Rev.* 97, 84–101.
717 <https://doi.org/10.1016/j.quascirev.2014.05.005>
- 718 Gaillardet, J., Dupré, B., Louvat, P., Allègre, C.J., 1999. Global silicate weathering and CO
719 consumption rates deduced from the chemistry of large rivers. *Chem. Geol.* 159, 3–30.
720 [https://doi.org/http://dx.doi.org/10.1016/S0009-2541\(99\)00031-5](https://doi.org/http://dx.doi.org/10.1016/S0009-2541(99)00031-5)
- 721 Garcin, Y., Junginger, A., Melnick, D., Olago, D.O., Strecker, M.R., Trauth, M.H., 2009. Late
722 Pleistocene-Holocene rise and collapse of Lake Suguta, northern Kenya Rift. *Quat. Sci.
723 Rev.* 28, 911–925. <https://doi.org/10.1016/j.quascirev.2008.12.006>
- 724 Garzanti, E., Andò, S., Padoan, M., Vezzoli, G., El Kammar, A., 2015. The modern Nile
725 sediment system: Processes and products. *Quat. Sci. Rev.* 130, 9–56.
726 <https://doi.org/10.1016/j.quascirev.2015.07.011>
- 727 Genske, F.S., Turner, S.P., Beier, C., Chu, M.F., Tonarini, S., Pearson, N.J., Haase, K.M.,
728 2014. Lithium and boron isotope systematics in lavas from the Azores islands reveal
729 crustal assimilation. *Chem. Geol.* 373, 27–36.
730 <https://doi.org/10.1016/j.chemgeo.2014.02.024>
- 731 Gislason, S.R., Arnorsson, S., Armannsson, H., 1996. Chemical weathering of basalt as

- 732 deduced from the composition of precipitation, rivers and rocks in SW Iceland. *Am. J.*
733 *Sci.* 296, 837–907.
- 734 Gislason, S.R., Oelkers, E.H., 2003. Mechanism, rates, and consequences of basaltic glass
735 dissolution: II. An experimental study of the dissolution rates of basaltic glass as a
736 function of pH and temperature. *Geochim. Cosmochim. Acta* 67, 3817–3832.
737 [https://doi.org/10.1016/S0016-7037\(00\)00176-5](https://doi.org/10.1016/S0016-7037(00)00176-5)
- 738 Gislason, S.R., Oelkers, E.H., Eiriksdottir, E.S., Kardjilov, M.I., Gisladottir, G., Sigfusson,
739 B., Snorrason, A., Elefsen, S., Hardardottir, J., Torssander, P., Oskarsson, N., 2009.
740 Direct evidence of the feedback between climate and weathering. *Earth Planet. Sci. Lett.*
741 277, 213–222. <https://doi.org/10.1016/j.epsl.2008.10.018>
- 742 Godd ris, Y., Brantley, S.L., Fran ois, L.M., Schott, J., Pollard, D., D qu , M., Dury, M.,
743 2013. Rates of consumption of atmospheric CO₂ through the weathering of loess during
744 the next 100 yr of climate change. *Biogeosciences* 10, 135–148.
745 <https://doi.org/10.5194/bg-10-135-2013>
- 746 Hoelzmann, P., Schwalb, A., Roberts, N., Cooper, P., Burgess, A., 2010. Hydrological
747 response of an east-Saharan palaeolake (NW Sudan) to early-Holocene climate.
748 *Holocene* 20, 537–549. <https://doi.org/10.1177/0959683609356584>
- 749 Hofmann, C., Courtillot, V., F raud, G., Rochette, P., Yirgus, G., Ketefo, E., Pik, R., 1998.
750 Timing of the Ethiopian flood basalt event and implications for plume birth and global
751 change. *Nature* 394, 192–195. <https://doi.org/10.1038/nature02336.1>
- 752 Huh, Y., Chan, L.H., Chadwick, O.A., 2004. Behavior of lithium and its isotopes during
753 weathering of Hawaiian basalt. *Geochemistry, Geophys. Geosystems* 5.
754 <https://doi.org/10.1029/2004GC000729>
- 755 Kisakurek, B., James, R.H., Harris, N.B.W., 2005. Li and $\delta^7\text{Li}$ in Himalayan rivers: Proxies
756 for silicate weathering? *Earth Planet. Sci. Lett.* 237, 387–401.
757 <https://doi.org/10.1016/j.epsl.2005.07.019>
- 758 Kisak rek, B., Widdowson, M., James, R.H., 2004. Behaviour of Li isotopes during
759 continental weathering: The Bidar laterite profile, India. *Chem. Geol.* 212, 27–44.
760 <https://doi.org/10.1016/j.chemgeo.2004.08.027>
- 761 Korecha, D., Barnston, A.G., 2007. Predictability of June–September Rainfall in Ethiopia.
762 *Mon. Weather Rev.* 135, 628–650. <https://doi.org/10.1175/MWR3304.1>
- 763 Lamb, H.F., Bates, C.R., Bryant, C.L., Davies, S.J., Huws, D.G., Marshall, M.H., Roberts,
764 H.M., 2018. 150,000-year palaeoclimate record from northern Ethiopia supports early,
765 multiple dispersals of modern humans from Africa. *Sci. Rep.* 8, 1–7.
766 <https://doi.org/10.1038/s41598-018-19601-w>
- 767 Lanckriet, S., Schwenninger, J.L., Frankl, A., Nyssen, J., 2015. The Late-Holocene
768 geomorphic history of the Ethiopian Highlands: Supportive evidence from May Tsimble.
769 *Catena* 135, 290–303. <https://doi.org/10.1016/j.catena.2015.08.011>
- 770 Lechler, M., Pogge von Strandmann, P.A.E., Jenkyns, H.C., Prosser, G., Parente, M., 2015.
771 Lithium-isotope evidence for enhanced silicate weathering during OAE 1a (Early Aptian
772 Selli event). *Earth Planet. Sci. Lett.* 432, 210–222.
773 <https://doi.org/10.1016/j.epsl.2015.09.052>
- 774 Leemans, Cramer, 1991. The IIASA Database for Mean Monthly Values of Temperature,

- 775 Precipitation, and Cloudiness on the Global Terrestrial Grid. International Institute for
776 Applied Systems Analysis, Laxenburg, Austria. 1991.
- 777 Lefebvre, V., Donnadieu, Y., Godd ris, Y., Fluteau, F., Hubert-Th ou, L., 2013. Was the
778 Antarctic glaciation delayed by a high degassing rate during the early Cenozoic? *Earth*
779 *Planet. Sci. Lett.* 371–372, 203–211. <https://doi.org/10.1016/j.epsl.2013.03.049>
- 780 Li, G., Elderfield, H., 2013. Evolution of carbon cycle over the past 100 million years.
781 *Geochim. Cosmochim. Acta* 103, 11–25. <https://doi.org/10.1016/j.gca.2012.10.014>
- 782 Li, G., Hartmann, J., Derry, L.A., West, A.J., You, C.F., Long, X., Zhan, T., Li, L., Li, G.,
783 Qiu, W., Li, T., Liu, L., Chen, Y., Ji, J., Zhao, L., Chen, J., 2016. Temperature
784 dependence of basalt weathering. *Earth Planet. Sci. Lett.* 443, 59–69.
785 <https://doi.org/10.1016/j.epsl.2016.03.015>
- 786 Li, S.L., Calmels, D., Han, G., Gaillardet, J., Liu, C.Q., 2008. Sulfuric acid as an agent of
787 carbonate weathering constrained by $\delta^{13}\text{CDIC}$: Examples from Southwest China. *Earth*
788 *Planet. Sci. Lett.* 270, 189–199. <https://doi.org/10.1016/j.epsl.2008.02.039>
- 789 Louvat, P., 1997. Etude g ochimique de l' rosion fluviale d'iles volcaniques   l'aide des
790 bilans d' l ments majeurs et traces. PhD Thesis Universit , 322pp.
- 791 Louvat, P., All gre, C.J., 1998. Riverrine erosion rates on Sao Miguek volcanic island, Azores
792 archipelago. *Chem. Geol.* 148, 177–200.
- 793 Louvat, P., All gre, C.J., 1998. Riverine erosion rates on Sao Miguel volcanic island, Azores
794 archipelago. USDA For. Serv. - Gen. Tech. Rep. RMRS-GTR 148, 177–200.
795 [https://doi.org/10.1016/S0009-2541\(98\)00028-X](https://doi.org/10.1016/S0009-2541(98)00028-X)
- 796 Louvat, P., All gre, C.J., 1997. Present denudation rates on the island of r union determined
797 by river geochemistry: Basalt weathering and mass budget between chemical and
798 mechanical erosions. *Geochim. Cosmochim. Acta* 61, 3645–3669.
799 [https://doi.org/10.1016/S0016-7037\(97\)00180-4](https://doi.org/10.1016/S0016-7037(97)00180-4)
- 800 Marzin, C., Braconnot, P., 2009. The role of the ocean feedback on Asian and African
801 monsoon variations at 6 kyr and 9.5 kyr BP. *Comptes Rendus - Geosci.* 341, 643–655.
802 <https://doi.org/10.1016/j.crte.2009.09.001>
- 803 MERID, F., 2005. National Nile Basin Water Quality Monitoring Baseline Report for
804 Ethiopia.
- 805 Meybeck, M., 1986. Composition chimique des ruisseaux non pollu s de France. *Sci. Geol.*
806 3–77.
- 807 Millot, R., Gaillardet, J., Dupr , B., All gre, C.J., 2002. The global control of silicate
808 weathering rates and the coupling with physical erosion. new insights from rivers Can.
809 *Shield* 196, 83–98.
- 810 Millot, R., Guerrot, C., Vigier, N., 2004. Accurate and high-precision measurement of lithium
811 isotopes in two reference materials by MC-ICP-MS. *Geostand. Geoanalytical Res.* 28,
812 153–159. <https://doi.org/10.1111/j.1751-908X.2004.tb01052.x>
- 813 Millot, R., Vigier, N., Gaillardet, J., 2010. Behaviour of lithium and its isotopes during
814 weathering in the Mackenzie Basin, Canada. *Geochim. Cosmochim. Acta* 74, 3897–
815 3912. <https://doi.org/10.1016/j.gca.2010.04.025>
- 816 Mohr, P, Z.B., 1988. The Ethiopian flood basalt province. McDougall, J.D. _Ed., *Cont. flood*

- 817 basalts. *Kluwer Acad. Publ., Dordr.* 63–110. [https://doi.org/10.1007/978-94-015-7805-](https://doi.org/10.1007/978-94-015-7805-9_3)
818 9_3
- 819 Négrel, P., Allègre, C.J., Dupré, B., Lewin, E., 1993. Erosion sources determined by inversion
820 of major and trace element ratios and strontium isotopic ratios in river water: the Congo
821 Basin case. *Earth Planet. Sci. Lett.* 120, 59–76.
- 822 Négrel, P., Deschamps, P., 1996. Natural and anthropogenic budgets of a small watershed in
823 the Massif Central (France): chemical and strontium isotopic characterization of water
824 and sediments. *Aquat. Geochem* 2, 1–27.
- 825 Nyssen, J., Vandenreyken, H., Poesen, J., Moeyersons, J., Deckers, J., Haile, M., Salles, C.,
826 Govers, G., 2005. Rainfall erosivity and variability in the Northern Ethiopian Highlands.
827 *J. Hydrol.* 311, 172–187. <https://doi.org/10.1016/j.jhydrol.2004.12.016>
- 828 Pik, R., Deniel, C., Coulon, C., Yirgu, G., Hofmann, C., Ayalew, D., 1998. The northwestern
829 Ethiopian Plateau flood basalts: classification and spatial distribution of magma types. *J.*
830 *Volcanol. Geotherm. Res.* 81, 91–111. [https://doi.org/10.1016/S0377-0273\(97\)00073-5](https://doi.org/10.1016/S0377-0273(97)00073-5)
- 831 Pik, R., Deniel, C., Coulon, C., Yirgu, G., Marty, B., 1999. Isotopic and trace element
832 signatures of Ethiopian flood basalts: Evidence for plume-lithosphere interactions.
833 *Geochim. Cosmochim. Acta* 63, 2263–2279. [https://doi.org/10.1016/S0016-](https://doi.org/10.1016/S0016-7037(99)00141-6)
834 7037(99)00141-6
- 835 Pik, R., Marty, B., Carignan, J., Lavé, J., 2003. Stability of the Upper Nile drainage network
836 (Ethiopia) deduced from (U-Th)/He thermochronometry: Implications for uplift and
837 erosion of the Afar plume dome. *Earth Planet. Sci. Lett.* 215, 73–88.
838 [https://doi.org/10.1016/S0012-821X\(03\)00457-6](https://doi.org/10.1016/S0012-821X(03)00457-6)
- 839 Pistiner, J.S., Henderson, G.M., 2003. Lithium-isotope fractionation during continental
840 weathering processes. *Earth Planet. Sci. Lett.* 214, 327–339.
841 [https://doi.org/10.1016/S0012-821X\(03\)00348-0](https://doi.org/10.1016/S0012-821X(03)00348-0)
- 842 Pogge von Strandmann, P.A.E., Frings, P.J., Murphy, M.J., 2017. Lithium isotope behaviour
843 during weathering in the Ganges Alluvial Plain. *Geochim. Cosmochim. Acta* 198, 17–31.
844 <https://doi.org/10.1016/j.gca.2016.11.017>
- 845 Pokrovsky, O.S., Schott, J., Kudryavtzev, D.I., Dupré, B., 2005. Basalt weathering in Central
846 Siberia under permafrost conditions. *Geochim. Cosmochim. Acta* 69, 5659–5680.
847 <https://doi.org/10.1016/j.gca.2005.07.018>
- 848 Revel, M., Colin, C., Bernasconi, S., Combourieu-Nebout, N., Ducassou, E., Grousset, F.E.,
849 Rolland, Y., Migeon, S., Bosch, D., Brunet, P., Zhao, Y., Mascle, J., 2014. 21,000 Years
850 of Ethiopian African monsoon variability recorded in sediments of the western Nile
851 deep-sea fan. *Reg. Environ. Chang.* 14, 1685–1696. [https://doi.org/10.1007/s10113-014-](https://doi.org/10.1007/s10113-014-0588-x)
852 0588-x
- 853 Revel, M., Ducassou, E., Grousset, F.E., Bernasconi, S.M., Migeon, S., Revillon, S., Mascle,
854 J., Murat, A., Zaragosi, S., Bosch, D., 2010. 100,000 Years of African monsoon
855 variability recorded in sediments of the Nile margin. *Quat. Sci. Rev.* 29, 1342–1362.
856 <https://doi.org/10.1016/j.quascirev.2010.02.006>
- 857 Revel, M., Ducassou, E., Skonieczny, C., Colin, C., Bastian, L., Bosch, D., Migeon, S.,
858 Mascle, J., 2015. 20,000 years of Nile River dynamics and environmental changes in the
859 Nile catchment area as inferred from Nile upper continental slope sediments. *Quat. Sci.*

- 860 Rev. 130. <https://doi.org/10.1016/j.quascirev.2015.10.030>
- 861 Riotte, J., Chabaux, F., Benedetti, M.F., Dia, A., Gérard, M., Boulégué, J., Etamé, J., 2003. U
862 colloidal transport and origin of the $^{234}\text{U}/^{238}\text{U}$ fractionation in surface waters: new
863 insights from Mount Cameroon. *Chem. Geol.* 202, 363–379.
- 864 Rochette, P., Tamrat, E., Féraud, G., Pik, R., Courtillot, V., Ketefo, E., Coulon, C., Hoffmann,
865 C., Vandamme, D., Yirgu, G., 1998. Magnetostratigraphy and timing of the Oligocene
866 Ethiopian traps. *Earth Planet. Sci. Lett.* 164, 497–510. [https://doi.org/10.1016/S0012-](https://doi.org/10.1016/S0012-821X(98)00241-6)
867 [821X\(98\)00241-6](https://doi.org/10.1016/S0012-821X(98)00241-6)
- 868 Rothacker, L., Dosseto, A., Francke, A., Chivas, A.R., Vigier, N., Kotarba-Morley, A.M.,
869 Menozzi, D., 2018. Impact of climate change and human activity on soil landscapes over
870 the past 12,300 years. *Sci. Rep.* 8, 1–7. <https://doi.org/10.1038/s41598-017-18603-4>
- 871 Ryu, J.S., Vigier, N., Lee, S.W., Lee, K.S., Chadwick, O.A., 2014. Variation of lithium
872 isotope geochemistry during basalt weathering and secondary mineral transformations in
873 Hawaii. *Geochim. Cosmochim. Acta* 145, 103–115.
874 <https://doi.org/10.1016/j.gca.2014.08.030>
- 875 Schmitt, A.D., Vigier, N., Lemarchand, D., Millot, R., Stille, P., Chabaux, F., 2012. Processes
876 controlling the stable isotope compositions of Li, B, Mg and Ca in plants, soils and
877 waters: A review. *Comptes Rendus - Geosci.* 344, 704–722.
878 <https://doi.org/10.1016/j.crte.2012.10.002>
- 879 Shanahan, T.M., Mckay, N.P., Hughen, K.A., Overpeck, J.T., Otto-Bliesner, B., Heil, C.W.,
880 King, J., Scholz, C.A., Peck, J., 2015. The time-transgressive termination of the African
881 humid period. *Nat. Geosci.* 8, 140–144. <https://doi.org/10.1038/ngeo2329>
- 882 Stallard, R.F., Edmond, J.M., 1983. Geochemistry of the Amazon. *J. Geophys. Res.* 88,
883 9671–9688.
- 884 Torres, M.A., West, A.J., Clark, K.E., Paris, G., Bouchez, J., Ponton, C., Feakins, S.J., Galy,
885 V., Adkins, J.F., 2016. The acid and alkalinity budgets of weathering in the Andes–
886 Amazon system: Insights into the erosional control of global biogeochemical cycles.
887 *Earth Planet. Sci. Lett.* 450, 381–391. <https://doi.org/10.1016/j.epsl.2016.06.012>
- 888 Tuenter, E., Weber, S.L., Hilgen, F.J., Lourens, L.J., 2003. The response of the African
889 summer monsoon to remote and local forcing due to precession and obliquity. *Glob.*
890 *Planet. Change* 36, 219–235. [https://doi.org/10.1016/S0921-8181\(02\)00196-0](https://doi.org/10.1016/S0921-8181(02)00196-0)
- 891 Verney-Carron, A., Vigier, N., Millot, R., 2011. Experimental determination of the role of
892 diffusion on Li isotope fractionation during basaltic glass weathering. *Geochim.*
893 *Cosmochim. Acta* 75, 3452–3468. <https://doi.org/10.1016/j.gca.2011.03.019>
- 894 Vigier, N., Bourdon, B., Lewin, E., Dupré, B., Turner, S., Chakrapani, G.J., van Calsteren, P.,
895 Allègre, C.J., 2005. Mobility of U-series nuclides during basalt weathering: An example
896 from the Deccan Traps (India). *Chem. Geol.* 219, 69–91.
897 <https://doi.org/10.1016/j.chemgeo.2005.02.010>
- 898 Vigier, N., Decarreau, A., Millot, R., Carignan, J., Petit, S., France-Lanord, C., 2008.
899 Quantifying Li isotope fractionation during smectite formation and implications for the
900 Li cycle. *Geochim. Cosmochim. Acta* 72, 780–792.
901 <https://doi.org/10.1016/j.gca.2007.11.011>
- 902 Vigier, N., Gislason, S.R., Burton, K.W., Millot, R., Mokadem, F., 2009. The relationship

903 between riverine lithium isotope composition and silicate weathering rates in Iceland.
904 *Earth Planet. Sci. Lett.* 287, 434–441. <https://doi.org/10.1016/j.epsl.2009.08.026>

905 Vigier, N., Godd eris, Y., 2015. A new approach for modeling Cenozoic oceanic lithium
906 isotope paleo-variations: The key role of climate. *Clim. Past* 11, 635–645.
907 <https://doi.org/10.5194/cp-11-635-2015>

908 von Strandmann, P.A.E.P., Burton, K.W., James, R.H., van Calsteren, P., Gislason, S.R.,
909 2010. Assessing the role of climate on uranium and lithium isotope behaviour in rivers
910 draining a basaltic terrain. *Chem. Geol.* 270, 227–239.
911 <https://doi.org/10.1016/j.chemgeo.2009.12.002>

912 von Strandmann, P.A.E.P., Burton, K.W., James, R.H., van Calsteren, P., Gislason, S.R.,
913 Mokadem, F., 2006. Riverine behaviour of uranium and lithium isotopes in an actively
914 glaciated basaltic terrain. *Earth Planet. Sci. Lett.* 251, 134–147.
915 <https://doi.org/10.1016/j.epsl.2006.09.001>

916 von Strandmann, P.A.E.P., Opfergelt, S., Lai, Y.J., Sigf usson, B., Gislason, S.R., Burton,
917 K.W., 2012. Lithium, magnesium and silicon isotope behaviour accompanying
918 weathering in a basaltic soil and pore water profile in Iceland. *Earth Planet. Sci. Lett.*
919 339–340, 11–23. <https://doi.org/10.1016/j.epsl.2012.05.035>

920 Walker, J.C.G., Hays, P.B., Kasting, J.F., 1981. Weathering rates in 106 gm km⁻² yr⁻¹ of
921 dissolved SiO₂. Parentheses signify. *J. Geophys. Res.* 86, 9776–9782.

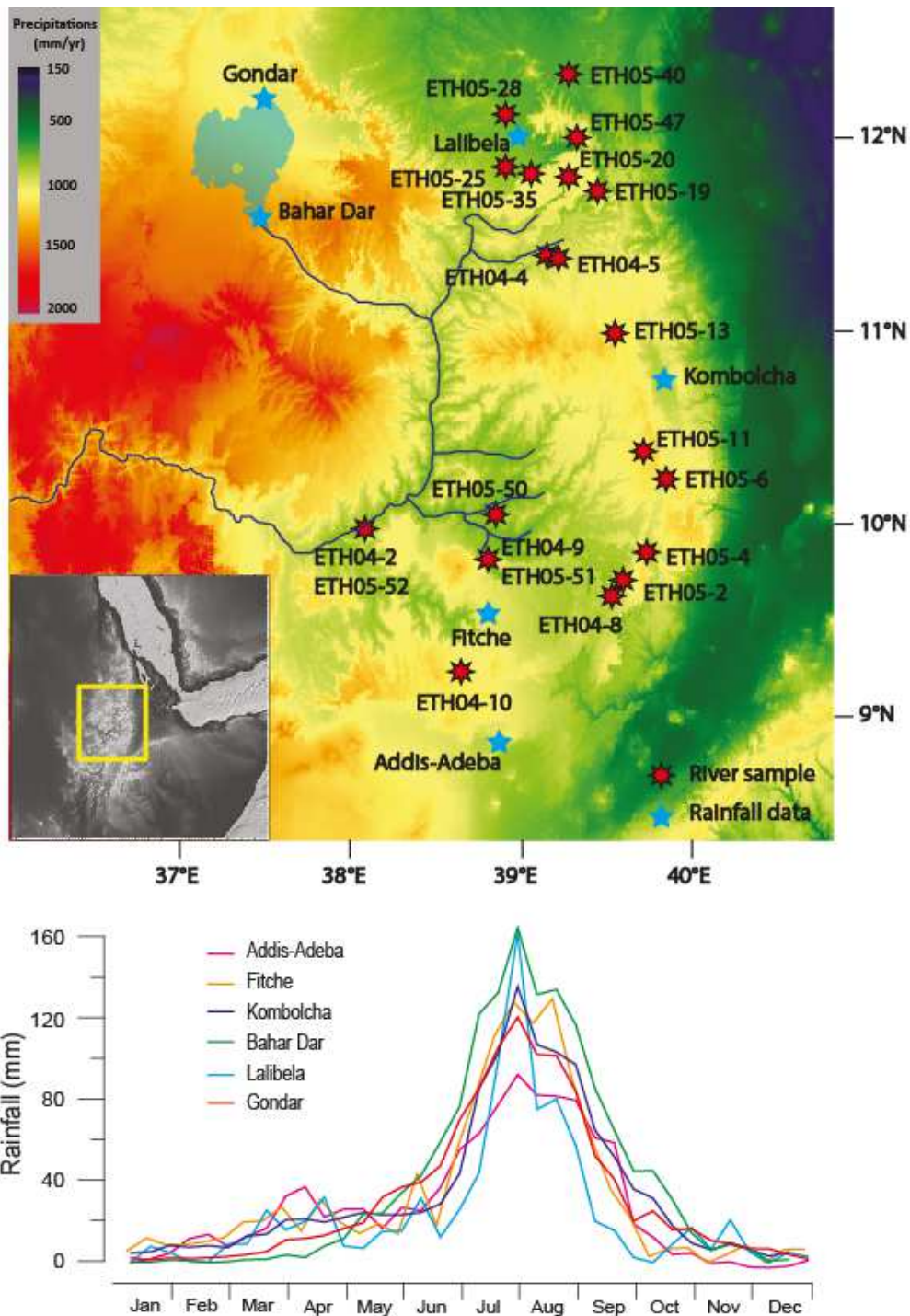
922 West, A.J., Galy, A., Bickle, M., 2005. Tectonic and climatic controls on silicate weathering.
923 *Earth Planet. Sci. Lett.* 235, 211–228. <https://doi.org/10.1016/j.epsl.2005.03.020>

924 Wimpenny, J., Gislason, S.R., James, R.H., Gannoun, A., Pogge Von Strandmann, P.A.E.,
925 Burton, K.W., 2010. The behaviour of Li and Mg isotopes during primary phase
926 dissolution and secondary mineral formation in basalt. *Geochim. Cosmochim. Acta* 74,
927 5259–5279. <https://doi.org/10.1016/j.gca.2010.06.028>

928 Wolfenden, E., Ebinger, C., Yirgu, G., Deino, A., Ayalew, D., 2004. Evolution of the
929 northern Main Ethiopian rift: Birth of a triple junction. *Earth Planet. Sci. Lett.* 224, 213–
930 228. <https://doi.org/10.1016/j.epsl.2004.04.022>

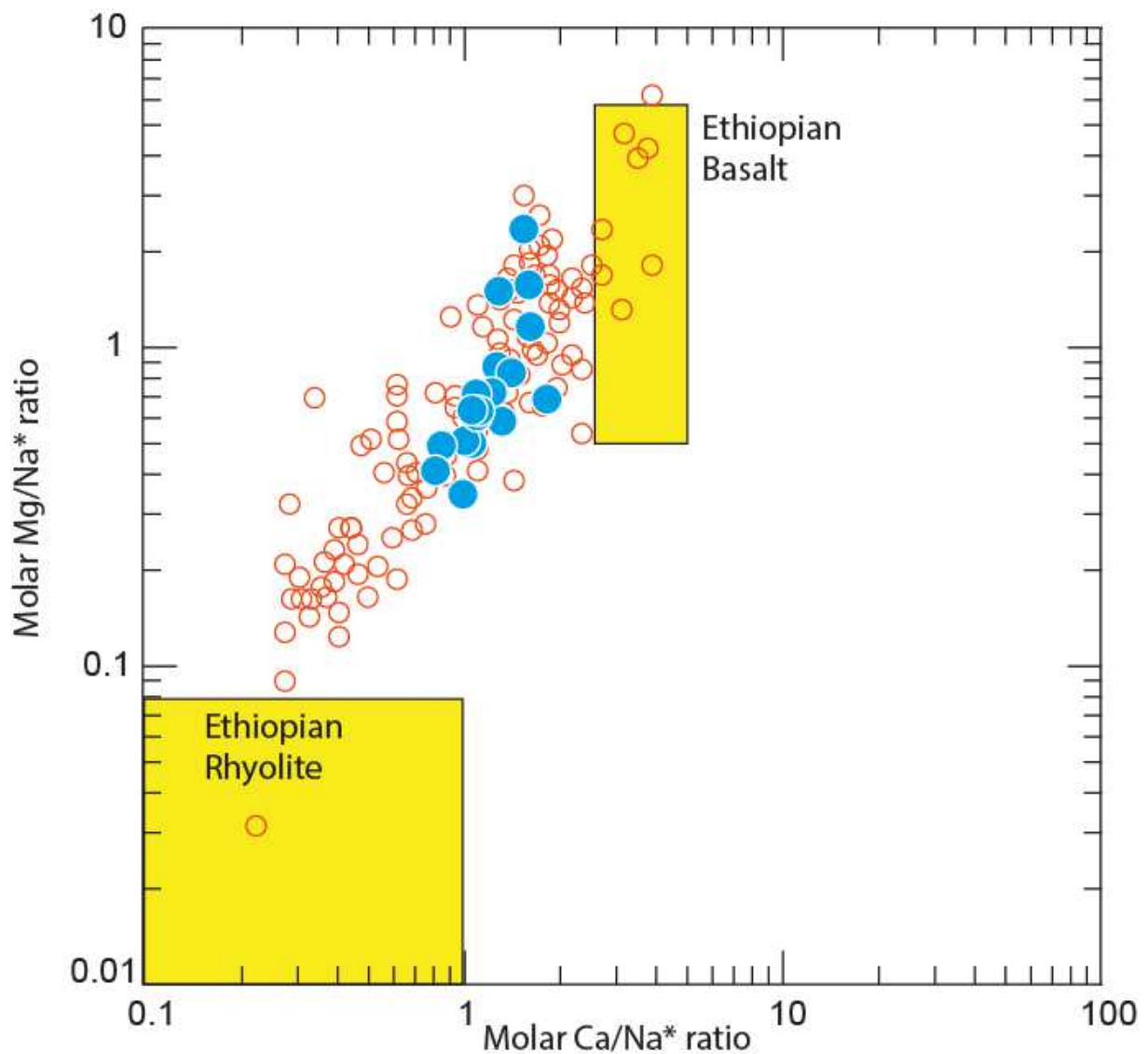
931 Zakharova, E.A., Pokrovsky, O.S., Dupr e, B., Zaslavskaya, M.B., 2005. Chemical weathering
932 of silicate rocks in Aldan Shield and Baikal Uplift: Insights from long-term seasonal
933 measurements of solute fluxes in rivers. *Chem. Geol.* 214, 223–248.
934 <https://doi.org/10.1016/j.chemgeo.2004.10.003>

935



938 Fig 1: A. Map showing samples localization and the studied area. Sample name on the map are: 1:
 939 Jara Wenz (ETH05-11); 2:Borkena Wenz (ETH05-13) ; 3: Robi Wenz (ETH05-4) ; 4: Meri Wenz
 940 (ETH05-28) ; 5: Tikur Wenz (ETH05-19) ; 6: Ketchin Abeba Wenz (ETH05-25) ; 7: Gereb Ara Wenz
 941 (ETH05-40) ; 8: Tekeze (ETH05-35) ; 9: Hormat Wenz (ETH05-47) ; 10: Ala-Wiha (ETH05-20) ; 11:
 942 Nazero Wenz (ETH05-6) .B. Measured rainfall (mm/week) temporal variations in various places of
 943 the Ethiopian Traps. Reported values corresponds to the average of rainfall between 1961 and 1997
 944 for Gondar, Bahar Dar, Kombolcha and Addis Ababa, between 1991 and 1997 for Fiche and between
 945 1994 and 1997 for Lalibellathe.

946
947

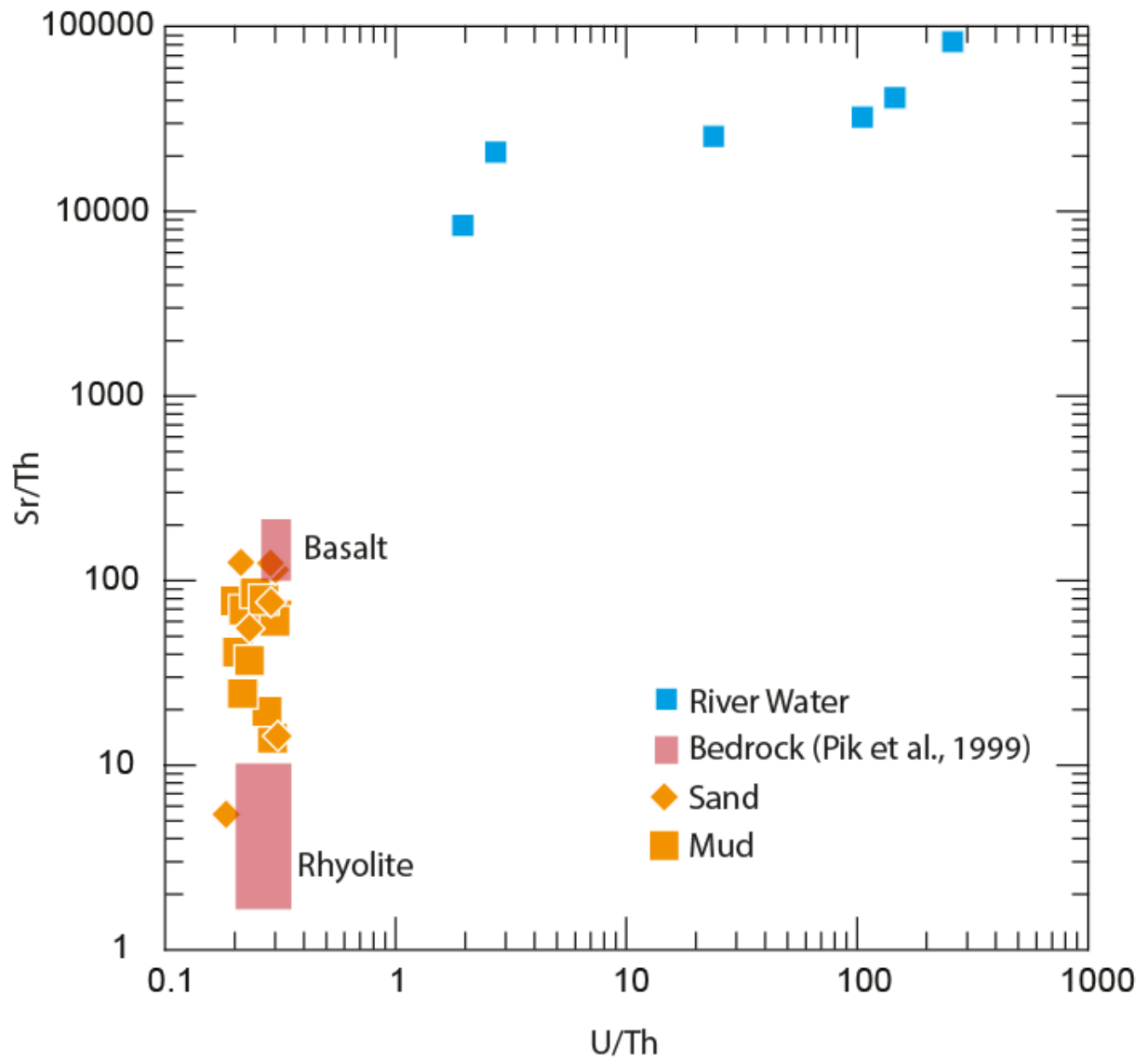


948

949 *Fig 2: Mg/Na molar ratio as a function of Ca/Na molar ratio, for river dissolved phases. Both ratios*
950 *are corrected from atmospheric inputs as described in section 4.2.1. The blue circles are for samples*
951 *analyzed in this study. Orange circles are for other basaltic regions reported in Dessert et al., (2003).*
952 *Bedrock data come from (Pik et al., 1999). (Benedetti et al., 1994; Dessert et al., 2001;*
953 *Gaillardet et al., 1999; Gislason et al., 1996; Leemans and Cramer, 1991; Louvat, 1997;*
954 *Pascale Louvat and Allègre, 1998; Louvat and Allègre, 1997; Meybeck, 1986; Nègre et al.,*
955 *1993; Nègre and Deschamps, 1996; Riotte et al., 2003)*

956

957



958 *Fig 3: Sr/Th as a function of U/Th (wt ratios) in the dissolved phases and solid phases of the sampled*
 959 *ivers. Bedrock values come from Pik et al., 1999.*

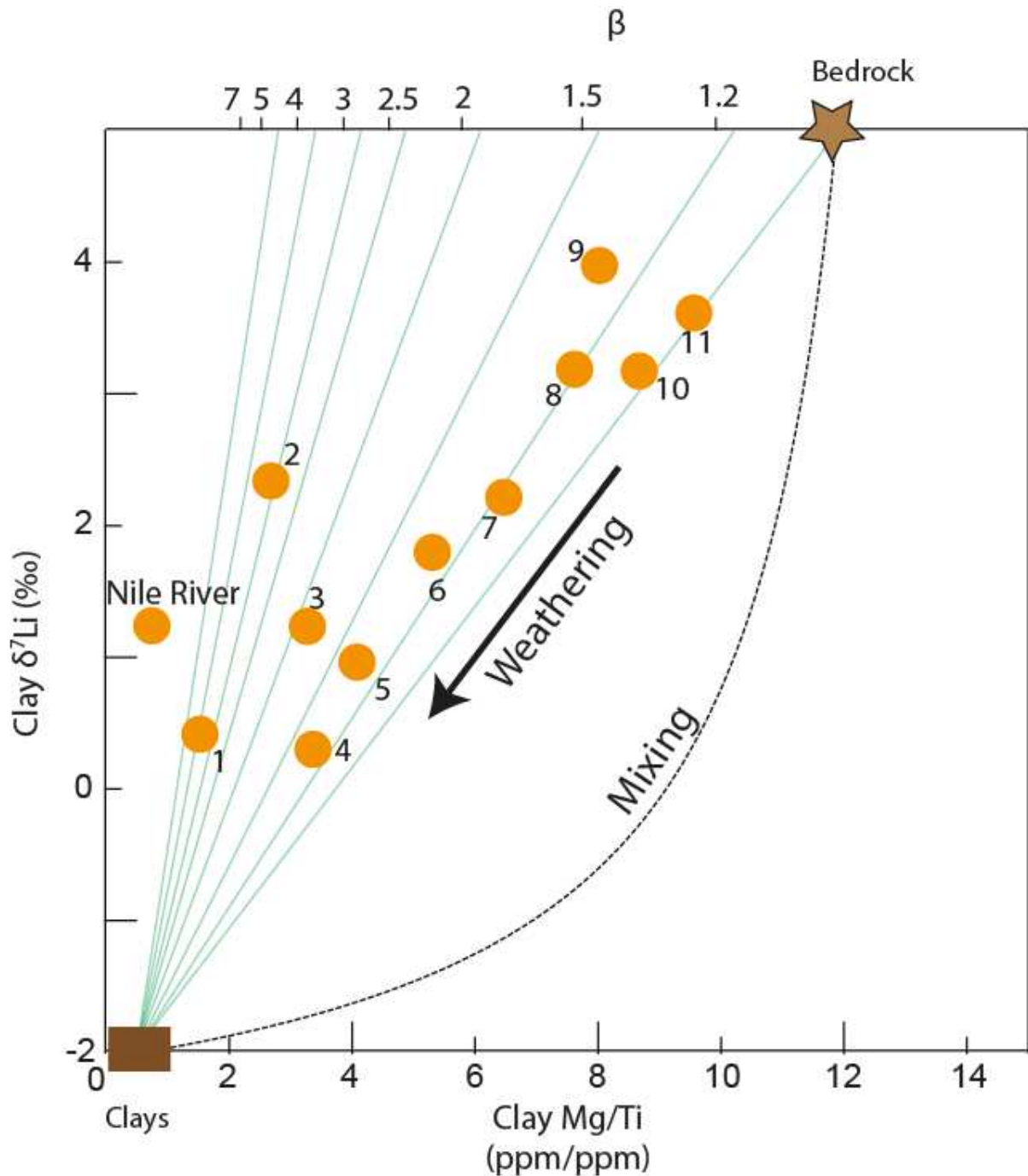
960

961

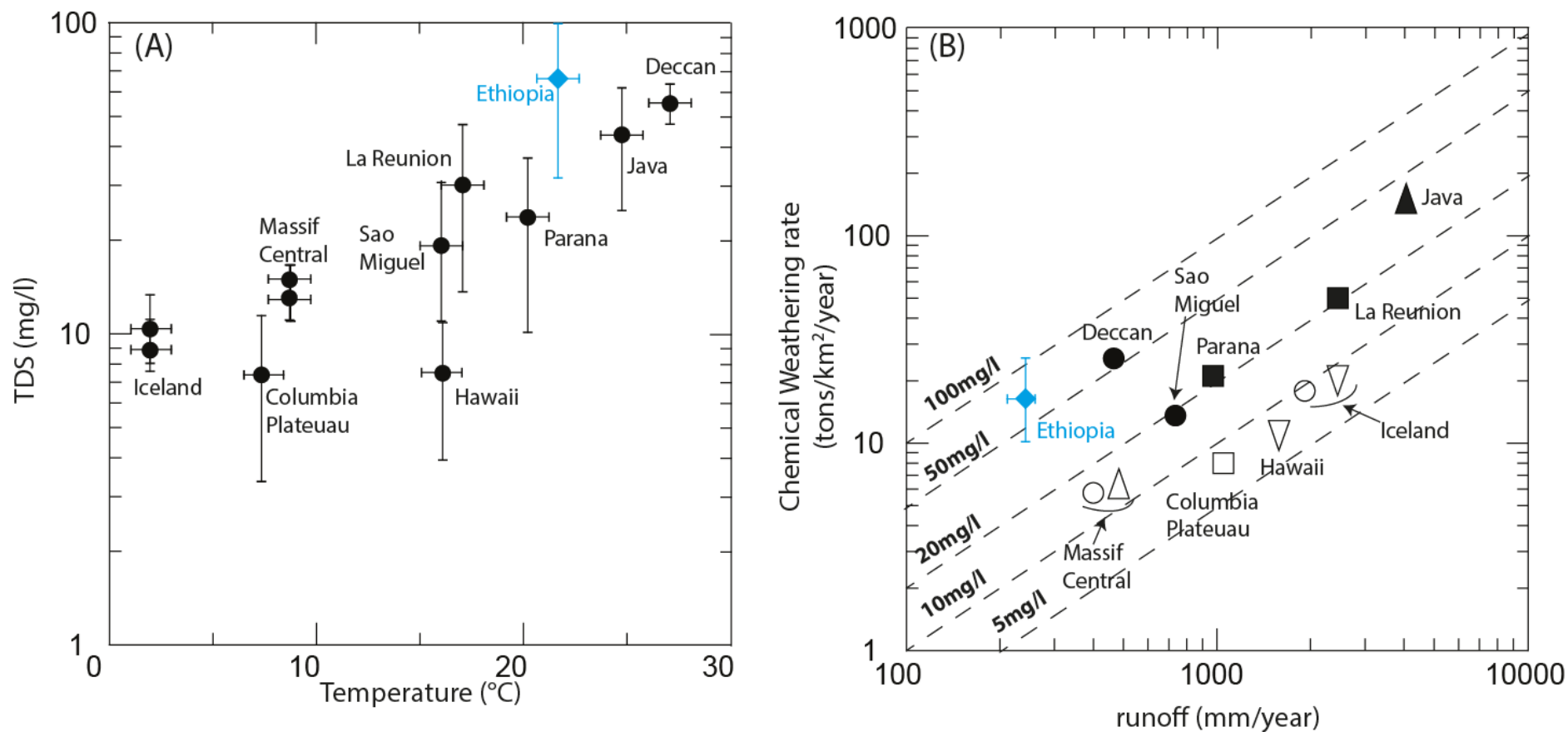
962

963

964

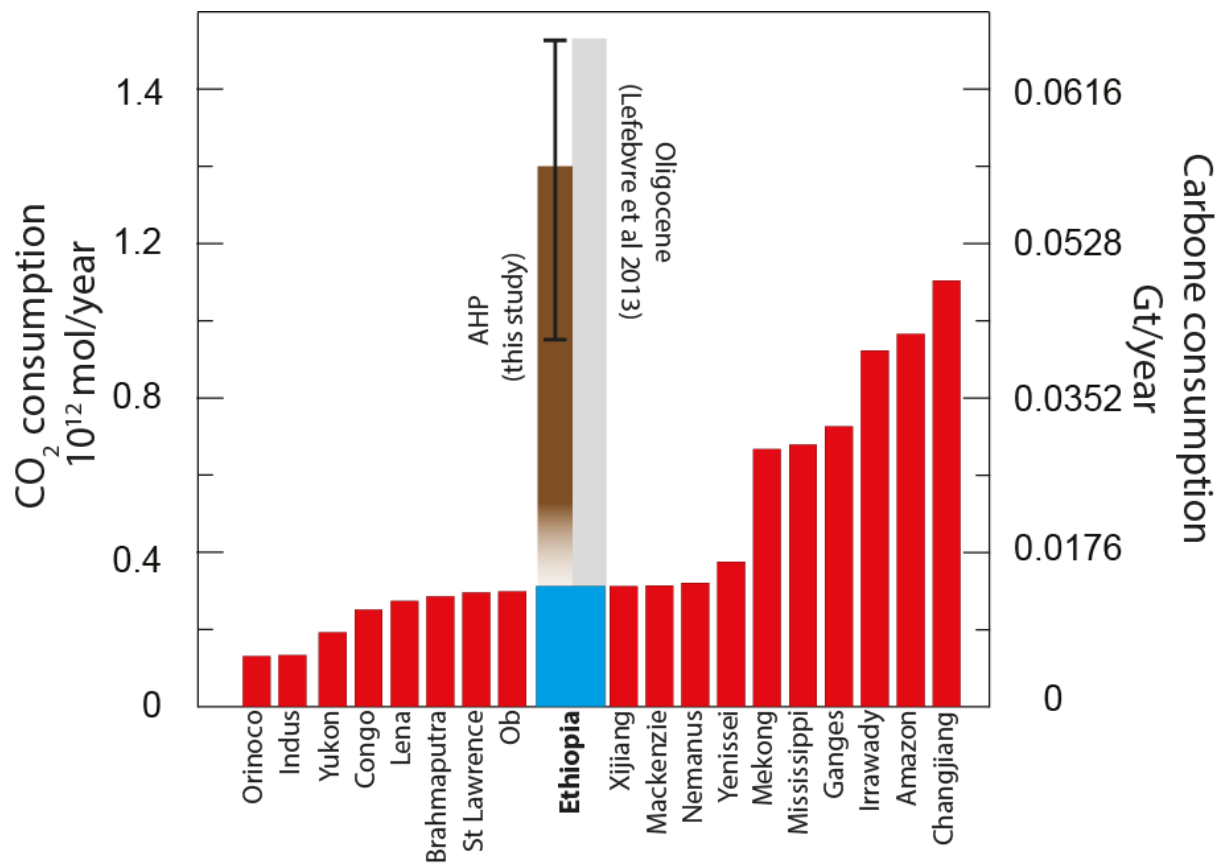


965
 966 Fig 4: Clay $\delta^7\text{Li}$ as a function of clay Mg/Ti for the main Blue Nile Basin rivers (blue
 967 diamonds). Green lines correspond to the result of the model described in section 5.1. for
 968 different β values. The dotted line corresponds to the theoretical mixing curve between
 969 bedrock and isotopically fractionated clay endmembers. Mixing model conditions: Bedrock
 970 $\delta^7\text{Li} = 5\text{‰}$, $[\text{Li}] = 10 \text{ ppm}$ (this study); clays $\delta^7\text{Li} = -2.3\text{‰}$ (clay $\delta^7\text{Li}$ measured in the most
 971 recent Nile delta fan sediments, $[\text{Li}] = 100 \text{ ppm}$ (Bastian, 2017; Bastian et al., 2017)).
 972 River numbers are the same as in figure 1.



973

974 *Fig 5: (A) TDS* (Total Dissolved Solids corrected for atmospheric inputs) as a function of temperature. The blue diamond corresponds to the*
 975 *Ethiopian Traps (average based on 17 data, see Table 3), and the black circles come from the compilation of (Dessert et al., 2003) (Benedetti et*
 976 *al., 1994; Dessert et al., 2001; Gaillardet et al., 1999; Gislason et al., 1996; Leemans and Cramer, 1991; Louvat, 1997; Pascale Louvat and*
 977 *Allègre, 1998; Louvat and Allègre, 1997; Meybeck, 1986; Nègrel et al., 1993; Nègrel and Deschamps, 1996; Riotte et al., 2003) and*
 978 *corresponds to most other basaltic areas studied thus far. (B) Plot of chemical erosion rate as a function of runoff (average based on 17 data,*
 979 *see Table 3). The blue diamond reflects the Ethiopian Traps (this study) and the other symbols come from (Dessert et al., 2003) and display other*
 980 *basaltic basins with active zones (in black) and inactive zone (in white). The dashed lines correspond to the TDS* concentrations.*



981

982 *Fig 6: Total CO₂ consumption in mol/year (Gaillardet et al., 1999) and annual CO₂*
 983 *consumption in GtC/yr due to silicate weathering for the largest rivers system. The blue bar*
 984 *corresponds to the current CO₂ consumption rate estimated in Ethiopia based on our*
 985 *measurements in river waters. The brown bar indicate the CO₂ consumption rate estimated*
 986 *for the African Humid Period (AHP, see text for more details, and the grey one is for the*
 987 *Oligocene and was published by (Lefebvre et al., 2013).*

988

989 *Table 1: Characteristics of the studied watersheds.*

990

991 *Table 2: Chemical composition of river waters, Total Dissolved Solid (TDS), silicate*
992 *weathering rate and related CO₂ consumption rate for the major basins of the Ethiopian*
993 *Traps.*

994 *Table 3: Chemical composition of sand, mud and clay samples (clay fractions have been*
995 *physically separated following the procedure described in part 3.3.2)*

996

997

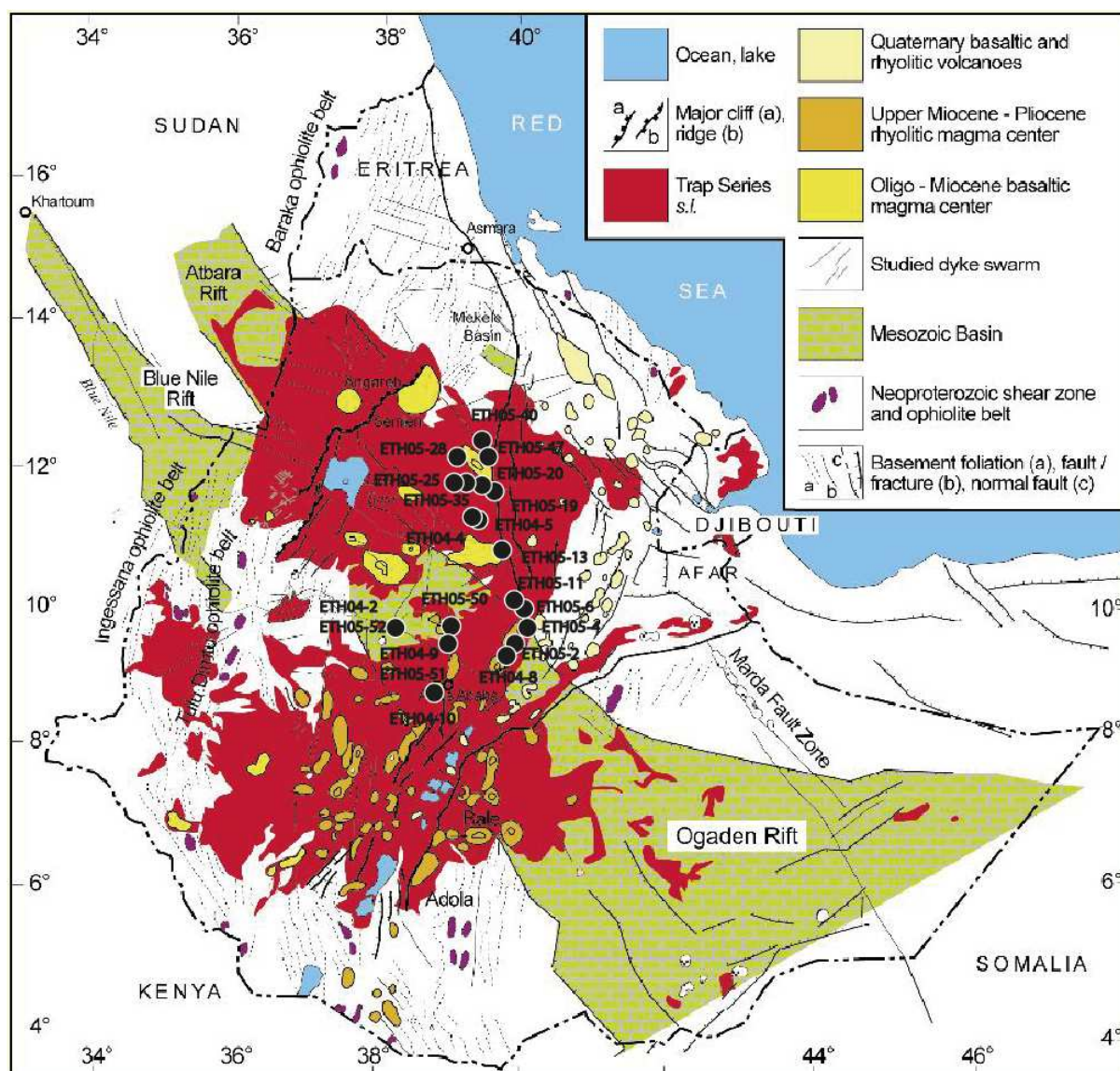
998

999

1000

1001

1002



1004 Fig S1: Ethiopian geological map. The black circles indicate our sampling sites.
 1005

1006 (https://esdac.jrc.ec.europa.eu/images/Eudasm/Africa/images/maps/download/afr_etgm.jpg)

1007

Table 1: Characteristics of the studied watersheds.

Sample number	Sample name	Elevation (m)	Mean elevation (m)	Area (km ²)	Annual discharge (m ³ /year)	calculated runoff (mm/an)
ETH04-2	Nil (Juin-04)	1158	2277	64214	1.8E+10	273
ETH 05 -52	Nil (Mars-05)	1158	2277	64214	1.8E+10	273
ETH04-9	Jemma Juin-04)	1290	2516	5878	1.4E+09	232
ETH05-51	Jemma (Mars-05)	1290	2516	5878	1.4E+09	232
ETH 05 -50	Wench't Wenz	1384	2520	2853	7.2E+08	252
ETH 05 -13	Borkena Wenz	1948	2658	24	6.5E+06	268
ETH 05 -19	Tikur Wiha (Woldia)	1729	2500	171	3.9E+07	227
ETH04-4	Wegel Tena	1651	2625	945	2.2E+08	234
ETH04-5	Bashillo	1649	2719	2668	7.1E+08	266
ETH05-40	Gereb Ara Wenz	1496	2243	58	1.1E+07	190
ETH05-20	Ala Wiha (Godg Wabit)	2028	2874	75	1.6E+07	218
ETH05-47	Hormat Wenz	1523	2346	134	2.7E+07	200
ETH 05 -25	Ketchin Abeba Wenz	1998	2848	220	4.8E+07	220
ETH 05 -28	Meri Wenz	2005	2591	131	2.6E+07	198
ETH 05 -35	Tekeze amont	2133	3020	493	1.1E+08	219
ETH04-10	plateau-N-Addis	2486	2697	56	1.5E+07	265
ETH04-8	Plateau E-Addis	2880	3267	32	8.5E+06	267
ETH 05 -2	Ulet Wenz	3034	3250	4	1.1E+06	270
ETH 05 -4	Robi Wenz	1389	2071	219	5.5E+07	252
ETH 05 -11	Jara Wenz	1656	2575	77	2.0E+07	265
ETH 05 -6	Nazero Wenz	1422	1879	171	4.4E+07	259

Table 2: Chemical composition of river waters, Total Dissolved Solid (TDS), silicate weathering rate and CO₂ consumption rate for the major basins of the Ethiopian Traps

Sample number	Sample name	Si (μmol/l)	Mg (μmol/l)	Ca (μmol/l)	Na (μmol/l)	K (μmol/l)	Al (μmol/l)	Sr (μg/l)	Th (μg/l)	U (μg/l)	F ⁻ (μmol/l)	Cl ⁻ (μmol/l)	NO ₃ ⁻ (μmol/l)	SO ₄ ²⁻ (μmol/l)	Mg ⁺ (μmol/l)	Ca ⁺ (μmol/l)	Na ⁺ (μmol/l)	K ⁺ (μmol/l)	F ⁺ (μmol/l)	NO ₃ ⁺ (μmol/l)	SO ₄ ²⁺ (μmol/l)	HCO ₃ ⁺ (μmol/l)	TDS* (μmol/l)	TDS* (mg/l)	Total chemical weathering (tons/km ² /year)	CO ₂ (10 ⁶ mol/km ² /year)
ETH04-2	Nil (Juin-04)	142	304	530	494	70	3405	135	0.005	0.1	8.5	76	43	146	296	529	427	68	8.5	43	146	1808	1320	40.9	11.2	0.49
ETH 05 -52	Nil (Mars-05)	154	341	584	414	61	398	174	< L.D.	0.2	8.9	70	4	171	334	582	352	60	8.9	4	171	1897	1328	41.9	11.4	0.52
ETH04-9	Jemma Juin-04)	332	323	688	650	141	3946	162	0.011	0.6	12.2	116	100	252	311	686	548	139	12.2	100	252	2075	1683	53.1	12.4	0.48
ETH05-51	Jemma (Mars-05)	660	684	1173	959	98	93	371	< L.D.	0.5	17.7	127	14	269	671	1171	847	96	17.7	14	269	4070	2785	86.5	20.1	0.95
ETH 05 -50	Wench't Wenz	631	585	1035	1219	92	264	257	< L.D.	0.6	14.2	165	8	402	568	1032	1073	89	14.2	8	402	3551	2762	83.3	21.0	0.90
ETH 05 -13	Borkena Wenz	465	499	1334	734	59	26	265	< L.D.	0.3	8.5	345	292	125	464	1327	429	52	8.5	292	125	3546	2273	76.4	20.5	0.95
ETH 05 -19	Tikur Wiha (Woldia)	667	789	1110	688	70	198	237	< L.D.	0.9	9.7	138	115	98	775	1107	566	68	9.7	115	98	4089	2516	78.9	17.9	0.93
ETH04-4	Wegel Tena	639	775	1141	901	65	3625	236	0.006	0.8	9.1	273	77	272	748	1135	659	60	9.1	77	272	3880	2602	81.2	19.0	0.91
ETH04-5	Bashillo	498	663	1022	940	60	4823	227	0.007	0.7	10.1	164	16	182	647	1019	795	57	10.1	16	182	3809	2518	77.1	20.5	1.02
ETH 05 -25	Ketchin Abeba Wenz	526	1565	1357	1055	71	62	488	< L.D.	0.9	8.8	348	132	212	1530	1350	748	65	8.8	132	212	6039	3692	111.0	24.4	1.33
ETH 05 -28	Meri Wenz	473	1365	1386	869	69	458	672	< L.D.	0.5	9.2	184	11	880	1346	1382	706	65	9.2	11	880	4466	3500	106.9	21.2	0.89
ETH 05 -35	Tekeze amont	453	1768	1170	761	48	101	360	< L.D.	1.2	7.3	298	129	205	1739	1164	497	43	7.3	129	205	5826	3442	102.0	22.4	1.28
ETH04-10	plateau-N-Addis	197	169	304	273	56	443	115	< L.D.	0.0	7.7	52	154	22	164	303	228	55	7.7	154	22	1014	750	23.5	6.2	0.27
ETH04-8	Plateau E-Addis	153	88	160	147	51	3359	53	0.006	0.0	6.4	54	21	15	83	159	99	50	6.4	21	15	582	391	12.6	3.4	0.16
ETH 05 -2	Ulet Wenz	199	59	133	102	20	2225	44	0.002	0.0	5.1	15	26	27	57	133	89	20	5.1	26	27	406	299	9.5	2.6	0.11
ETH 05 -4	Robi Wenz	539	250	721	734	73	307	114	< L.D.	0.4	12.2	56	59	70	244	720	684	72	12.2	59	70	2478	1720	53.3	13.4	0.62
ETH 05 -6	Nazero Wenz	877	581	1161	1155	100	68	174	0.002	0.5	21.3	168	8	90	565	1158	1007	97	21.3	8	90	4354	2826	87.1	22.5	1.13

